ELSEVIER

Contents lists available at ScienceDirect

## Aerospace Science and Technology

journal homepage: www.elsevier.com/locate/aescte





# Towards the understanding of vortex breakdown for improved RANS turbulence modeling

Tony Di Fabbio\*, Karthick Rajkumar, Eike Tangermann, Markus Klein

Department of Aerospace Engineering, Institute of Applied Mathematics and Scientific Computing, University of the Bundeswehr Munich, Werner-Heisenberg-Weg 39, Neubiberg, 85577, Bayern, Germany

#### ARTICLE INFO

Communicated by Cummings Russell

Keywords: Leading-edge vortex Vortex breakdown Turbulence modeling Reynolds stress tensor Boussinesq assumption Turbulence kinetic energy

#### ABSTRACT

A triple-delta wing configuration in transonic conditions has been investigated numerically, explicitly focusing on the leading-edge vortices during sideslip flow. Several shock waves manifest over the fuselage, leading to vortex-shock interactions. The primary focus of the analysis centers on the vortex breakdown phenomenon and its underlying causes. The flow field obtained from different turbulence modeling approaches is compared. This study aims to identify the limitations of a standard one-equation model in dealing with such complex applications. It explores physical and modeling reasons leading to the model's inaccuracies. The impact of turbulence treatment on the numerical results is explored, discussing turbulence-related variables. A novel and straightforward modification to the one-equation turbulence model is then introduced and assessed compared to experimental and computational data. The proposed model appears promising for enhancing the accuracy of the one-equation Reynolds Averaged Navier-Stokes outcomes.

## 1. Introduction

Highly swept wings operating under extreme flight conditions exhibit complex flow fields that are challenging to predict numerically and analyze experimentally. These wings are typically employed in agile military and supersonic aircraft due to their favorable aerodynamic characteristics at high Mach numbers. Their aerodynamic behavior is primarily governed by the vortex-dominated flow generated at the swept leading edge. Therefore, a comprehensive understanding and precise prediction of the vortical flow system are crucial during the aircraft design process [1,2].

Research on leading-edge vortices of swept wings with low aspect ratios has been ongoing for decades [3–6]. Computational Fluid Dynamics (CFD) experts have been striving to numerically estimate the behavior of these intricate and challenging flow patterns [7,8]. However, despite considerable efforts, no universally applicable solution has been discovered. Therefore, it is essential to assess several turbulence treatments to determine their suitability for addressing these wing configurations' demanding requirements.

In many cases, reliable and realistic results have been achieved by employing numerical simulations with eddy-viscosity-based Reynolds-averaged Navier-Stokes (RANS) models [9–12]. Nevertheless, while classical RANS models are highly efficient in computational time, they

often fall short in accurately predicting highly vortical flows in applications with high angles of attack (AoA) and sideslip [13–16]. This has sparked continuous interest in academia and industry to enhance the predictive accuracy of RANS models, especially in the aerospace field.

The complex turbulence fluctuations within the flow field, as captured by the underlying turbulence models, are represented by the Reynolds-stress tensor. Various assumptions are employed to model this tensor, categorizing the type of turbulence model. The widely accepted Boussinesq assumption linearly relates the stress tensor to velocity gradients through turbulent viscosity. However, due to the simplification of the Reynolds-stress tensor, this approach may not effectively predict vortical flows where stress and strain rates are not aligned or rapid redistribution among the stresses occurs [17]. Hence, it may not accurately capture high angle of attack and sideslip conditions. The literature presents then different methods to overcome the limitations of the linear RANS approach [14,18,19]. Pope [20] introduces a more realistic effective-viscosity formulation, and the Quadratic Constitutive Relation (QCR) [21] employs a nonlinear turbulent stress/strain equation, contrasting with the linear Boussinesq relation. These approaches account for the anisotropy property of Reynolds normal stresses, addressing their incorrect behavior.

Resolving turbulence using Direct Numerical Simulation or Large Eddy Simulation (LES) methods is computationally expensive and not

E-mail address: tony.difabbio@unibw.de (T. Di Fabbio).

<sup>\*</sup> Corresponding author.

#### Nomenclature AoA Angles of Attack Turbulent eddy viscosity ...... kg/(ms) $\mu_t$ Kinematic eddy viscosity..... m<sup>2</sup>/s QCR Quadratic Constitutive Relation $v_t$ Hi-Fi High-Fidelity Ω Rotation rate tensor magnitude . . . . . . 1/s SAnegRC Spalart-Allmaras One-Equation Model with negative tur-Q bulent viscosity and Rotation/Curvature correction $R_t$ Turbulent eddy viscosity over dynamic molecular $k\omega$ SST Menter $k - \omega$ Shear Stress Transport viscosity ..... -**IDDES** Improved Delayed Detached Eddy Simulation Reynolds number ..... ReSAS Scale Adaptive Simulation Density..... kg/m<sup>3</sup> **ADS** Airbus Defence And Space Angle of attack ...... o PΚ Production k Side slip angle..... o CTU Convective Time Unit CFL Courant-Friedrichs-Lewy number Symbols Velocity magnitude . . . . . m/s Free-stream velocity ..... m/s $C_L$ Lift coefficient . . . . ã Hybrid length scale ..... m Rolling moment coefficient..... - $C_{m_x}$ Modified SA eddy viscosity ...... m<sup>2</sup>/s $C_{m_{v}}$ Pitching moment coefficient..... -VCell volume..... m<sup>3</sup> $\delta_{ij}$ Kronecker delta ..... -RANS length scale ..... m $\Delta$ Characteristic cell size ..... m $W_{ij} \\ \tau_{ij}^R$ Rotation rate tensor ...... 1/s Time step size..... s $\Delta t$ Reynolds stress tensor . . . . Pa Normalized helicity ..... - $H_n$ $Turbulent \ kinetic \ energy..... \ m^2/s^2$ $\tau_{ij}$ Normalized Revnolds stress tensor..... k b Wing span . . . . . m $k_{SA}$ SA turbulent kinetic energy . . . . . . $m^2/s^2$ Pressure coefficient ..... $k_n$ Normalized turbulent kinetic energy ..... -LVelocity components..... m/s Characteristic length . . . . . m u, v, wCartesian coordinates . . . . . m Max, y, zDynamic molecular viscosity ...... kg/(ms) Dimensionless Cartesian coordinates ..... - $\xi, \eta, \psi$

feasible for routine applications. Consequently, high-fidelity (Hi-Fi) predictions of such complex configurations can only be performed for selected cases using hybrid RANS/LES approaches.

In this study, the flow around the triple-delta wing ADS-NA2-W1 [22] has been analyzed. This configuration features a sharp leading edge, which results in fixed flow separation, marking the initial stage of vortex formation. Consequently, the primary challenge lies in accurately modeling the formation and further development of the vortical flow system along the wing surface.

The simulations have been conducted under transonic and side slip conditions, with a Mach number  $(Ma_{\infty})$  of 0.85, Reynolds number  $(Re_{\infty})$  of  $12.53\times10^6$ , and sideslip angle  $(\beta)$  at  $5^{\circ}$ . Several angles of attack  $(\alpha)$  have been investigated, and the corresponding aerodynamic coefficients will be presented. The results from five different simulations featuring different turbulence model approaches are presented. These include Unsteady Reynolds-Averaged Navier-Stokes (URANS) simulations based on the Spalart-Allmaras One-Equation Model with corrections for negative turbulent viscosity and rotation/curvature correction (SAnegRC) [23,24], the Menter  $k\omega$ -SST model  $(k\omega$ SST) [25], as well as results from the scale-resolving simulation hybrid RANS/LES (IDDES) [26] and the scale-adaptive simulation (SAS) [27]. These approaches primarily differ in treating turbulent fluctuations, impacting solution accuracy and computational requirements.

This research also introduces a novel and straightforward modification to the one-equation RANS turbulence model, designated PK, representing Production-k (turbulent kinetic energy). The fifth simulation presents the results obtained using PK, developed based on the existing SAnegRC model. The Boussinesq assumption is modified by adding a model for the turbulent kinetic energy to be included in the one-equation model, which does not account for its modeling. The PK results are subsequently compared with current state-of-the-art outcomes to demonstrate enhanced accuracy. The numerical results

are validated using experimental data provided by Airbus Defence and Space (ADS) [22].

Given the transonic nature of the flow, multiple shock waves are observed across the fuselage, generating vortex-shock interactions and vortex breakdown phenomena. Particular attention will be given to the outcomes at  $\alpha = 20^{\circ}$ , due to the significant impact of the breakdown on the flow physics of the windward wing. This investigation predominantly concentrates on exploring the occurrence of vortex breakdown and its contributory factors. It aims to discern and correct the limitations of one-equation models when applied to delta wing flows. The Spalart-Allmaras model is a standard RANS closure for aerodynamic applications within the industrial sector, especially for its simplicity and robustness. Enhancing the model requires a deep understanding and thorough analysis of the root causes behind its inaccurate predictions. Both physical and modeling reasons contributing to these discrepancies are examined. The investigation also explores the influence of turbulence treatment on CFD results, elucidating the role of turbulencerelated variables.

#### 2. Turbulence modeling

The CFD simulations have been conducted using the DLR TAU-Code. A brief introduction to the code, along with an overview describing its functionality, has been provided by Gerhold [28]. Using a finite volume formulation, the TAU flow solver addresses the solution of the compressible, three-dimensional, unsteady Reynolds-Averaged or filtered Navier-Stokes equations. The governing equations have been detailed in the work of Langer et al. [29], and for the sake of brevity, they will not be presented here in full. Instead, the RANS equations and their closure through various turbulence approaches are introduced. They are crucial for justifying the achieved results and proposing potential improvements to the Spalart-Allmaras model.

#### 2.1. RANS equations and Boussinesa assumption

The RANS equations represent time-averaged equations of motion for fluid flow and constitute a transformed version of the general Navier-Stokes equations. The averaged solution is separated from the time-varying fluctuations within the system, with the latter accounting for turbulence in various flow conditions [30]. In the case of a stationary flow of an incompressible Newtonian fluid, the RANS equations can be expressed in Einstein notation within Cartesian coordinates as follows<sup>1</sup>

$$\rho \bar{u}_{j} \frac{\partial \bar{u}_{i}}{\partial x_{i}} = \rho \bar{f}_{i} + \frac{\partial}{\partial x_{j}} \left[ -\bar{p} \delta_{ij} + \mu \left( \frac{\partial \bar{u}_{i}}{\partial x_{j}} + \frac{\partial \bar{u}_{j}}{\partial x_{i}} \right) - \rho \overline{u'_{i} u'_{j}} \right]. \tag{1}$$

The left-hand side of this equation accounts for the alteration in the mean momentum of a fluid element due to the convection by the mean flow. This alteration is counterbalanced by several factors, including the mean body force, the isotropic stress attributed to the mean pressure field, the viscous stresses, and the apparent stress  $\left(-\rho u_i^\prime u_j^\prime\right)$  arising from the fluctuating velocity field, commonly known as the Reynolds stress. The nonlinear nature of the Reynolds stress term necessitates additional modeling to close the RANS equation for solution, resulting in the development of various turbulence models. Boussinesq postulated that the momentum transfer caused by turbulent eddies could be modeled using an eddy viscosity [32]. Boussinesq's assumption equates the Reynolds stress tensor, denoted as  $\tau_{ij}^R$ , to laminar-like stress terms. It states that the Reynolds stress tensor is proportional to the trace-less mean strain rate tensor, represented as  $S_{ij}^*$ , and can be expressed as follows

$$-\rho \overline{u'_i u'_j} = \tau_{ij}^R = 2 \,\mu_t \, S_{ij}^* - \frac{2}{3} \rho k \delta_{ij}, \tag{2}$$

where  $\mu_t$  is the eddy viscosity and  $S_{ij}^* = S_{ij} - \frac{1}{3} \frac{\partial u_k}{\partial x_k} \delta_{ij}$  with  $S_{ij} = \frac{1}{2} \left( \frac{\partial u_i}{\partial x_i} + \frac{\partial u_j}{\partial x_i} \right)$ .

## 2.2. One-equation model: SA-based URANS and IDDES

The Spalart-Allmaras model for eddy viscosity turbulence is built around a solitary transport equation for the eddy viscosity variable,  $v_t$ . The eddy viscosity establishes a linear relation  $-\overline{u_i u_j} = v_t S_{ij}$ , aligning with the Boussinesq assumption in Eq. (2). Contrary to certain two-equation models, the k term is neglected. A comprehensive analysis of the SA model is provided in Appendix A.

The model's equation for the modified eddy viscosity,  $\tilde{v}$ , is presented in its incompressible form as follows<sup>2</sup>

$$\frac{\partial \tilde{v}}{\partial t} + u_j \frac{\partial \tilde{v}}{\partial x_j} = c_{b1} \left( 1 - f_{t2} \right) \tilde{S} \tilde{v} - \left[ c_{w1} f_w - \frac{c_{b1}}{\kappa^2} f_{t2} \right] \left( \frac{\tilde{v}}{d} \right)^2 \tag{3}$$

$$+\frac{1}{\sigma} \left[ \frac{\partial}{\partial x_i} \left( (\nu + \tilde{\nu}) \frac{\partial \tilde{\nu}}{\partial x_i} \right) + c_{b2} \frac{\partial \tilde{\nu}}{\partial x_i} \frac{\partial \tilde{\nu}}{\partial x_i} \right]. \tag{4}$$

The production term depends on

$$\tilde{S} = \Omega + \frac{\tilde{v}}{\kappa^2 d^2} f_{\nu 2},\tag{5}$$

with the vorticity magnitude  $\Omega = \sqrt{2W_{ij}W_{ij}}$  computed from the vorticity tensor  $W_{ij} = \frac{1}{2}\left(\frac{\partial u_i}{\partial x_j} - \frac{\partial u_j}{\partial x_i}\right)$ .

The SAneg model is the same as the "standard" version (SA) when the turbulence variable  $\tilde{v}$  is greater than or equal to zero [23]. When  $\tilde{v}$  is negative since it is non-physical, it needs to be avoided, and the following equation is solved instead

$$\frac{\partial \tilde{v}}{\partial t} + u_j \frac{\partial \tilde{v}}{\partial x_i} = c_{b1} (1 - c_{t3}) \Omega \tilde{v} + c_{w1} f_w \left(\frac{\tilde{v}}{d}\right)^2$$
 (6)

$$+\frac{1}{\sigma} \left[ \frac{\partial}{\partial x_i} \left( (v + \tilde{v}) \frac{\partial \tilde{v}}{\partial x_i} \right) + c_{b2} \frac{\partial \tilde{v}}{\partial x_i} \frac{\partial \tilde{v}}{\partial x_i} \right]. \tag{7}$$

The production term becomes positive because the coefficient  $c_{t3}$  being set at 1.2. Indeed, the factors multiplying  $\tilde{v}$  and  $\tilde{v}$  itself are negative.

Shur et al. [24] additionally proposed a streamline curvature correction (SA-RC), which alters the production term with the rotation function

$$f_{r1} = (1 + c_{r1}) \frac{2r^*}{1 + r^*} \left[ 1 - c_{r3} \tan^{-1}(c_{r2}\tilde{r}) \right] - c_{r1}.$$
 (8)

The Spalart-Allmaras One-Equation Model with corrections for negative turbulent viscosity and rotation/curvature correction (SAnegRC) is applied in the URANS simulations.<sup>3</sup>

The IDDES method based on the Spalart-Allmaras One-Equation Model with corrections for negative turbulent viscosity (SAneg) is applied in the scale-resolving computations [26]. The RC modification is used just within the URANS computations since, in IDDES, the vortices are located in the LES zone. The IDDES approach has been selected for the scale-resolving simulations because, on a sharp leading-edge delta wing, turbulence usually starts soon after the leading-edge separation in the separated shear-layer yet close to the wall. The IDDES model essentially switches to URANS mode in the wall layer while running in LES mode in the off-wall region. Mesh refinement in the onset of the turbulent shear-layer emanating from the leading edge helps to drive the IDDES model into wall-modeled LES mode and thereby benefits from its capability of controlling the transition between RANS and LES in the region immediately after separation by trying to mitigate the grey-area effects [16,34].

As written in Eq. (4), in the Spalart-Allmaras-based RANS model, the turbulence length scale is the nearest wall distance,  $d=L_{RANS}=d_w$ , whereas the IDDES model, d is replaced with  $\tilde{d}=L_{IDDES}$ , defined as follows

$$\tilde{d} = \tilde{f}_d(1 + f_e)d + (1 + \tilde{f}_d)C_{DES}\Psi\Delta, \tag{9}$$

featuring several fitted functions and coefficients of great complexity, which can be found in literature [35].

#### 2.3. Two-equation model: $k\omega$ -based URANS and SAS

The scale-adaptive simulation is a method to allow the partial resolution of turbulence structures in unsteady flows [27]. The SAS model can be considered a URANS model with a scale-resolving capability, showing LES-like behavior. Unlike LES, it also remains well-defined if the mesh cells become coarser. In this model, the von Kármán length scale is introduced into the scale-determining equation, which lets the model dynamically switch from RANS to LES-like behavior in unsteady regions of the flow field. The employed SAS method is based on the Menter  $k-\omega$  SST model [25]. Within this model, the solution of the transport equations for turbulent kinetic energy k (Eq. (10))

<sup>&</sup>lt;sup>1</sup> A density-based average, known as the Favre average, is introduced if the Reynolds average is applied to the compressible form of the Navier–Stokes equations [31]. Here, the incompressible and stationary RANS are shown for simplification and conciseness.

<sup>&</sup>lt;sup>2</sup> The original SA model, in which density does not appear, applies to both incompressible and compressible flows, and it should be considered the standard form for compressible. However, an equivalent conservation form can be constructed by combining SA with the mass conservation equation [23].

<sup>&</sup>lt;sup>3</sup> For a comprehensive understanding of the SA one-equation turbulence model and its various modifications, refer to relevant literature [33,18,24,23]. This will provide deeper insights into the model's development and application in different flow scenarios.

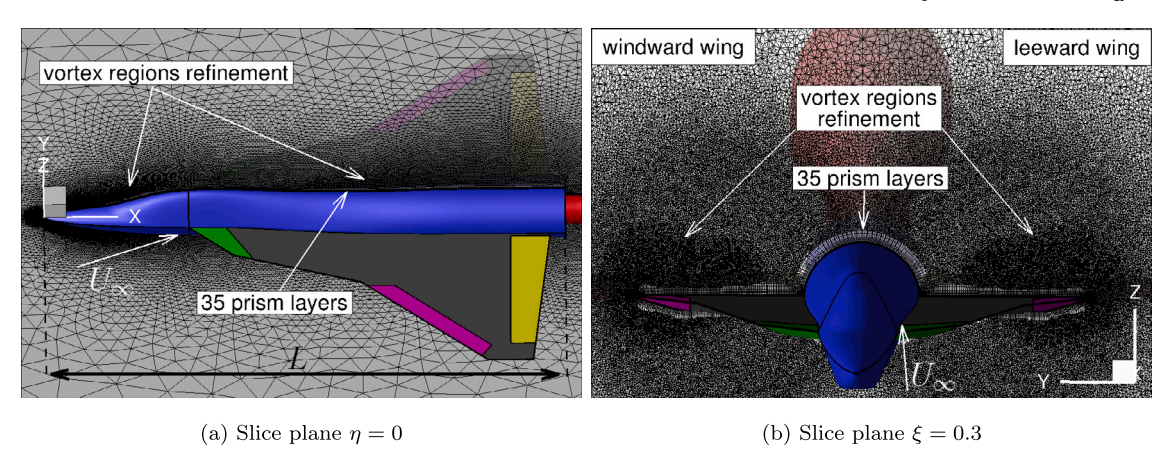


Fig. 1. Visualization of the ADS-NA2-W1 triple-delta wing geometry and mesh.

and dissipation rate  $\omega$  (Eq. (11)) yields the eddy viscosity as follows  $\mu_t = \frac{\rho a_1 k}{\max(a_1 \omega_1 Q E_n)}$ .

$$\frac{\partial \rho k}{\partial t} + u_i \frac{\partial \rho k}{\partial x_i} = P_{k\omega} - \beta^* \rho \omega k + \frac{\partial}{\partial x_i} \left[ \left( \mu + \sigma_{k1} \mu_t \right) \frac{\partial k}{\partial x_i} \right]$$
 (10)

$$\frac{\partial \rho \omega}{\partial t} + u_i \frac{\partial \rho \omega}{\partial x_i} = \frac{\gamma_1}{v_t} P_{k\omega} - \beta_1 \rho \omega^2 + \frac{\partial}{\partial x_j} \left[ \left( \mu + \sigma_{\omega 1} \mu_t \right) \frac{\partial \omega}{\partial x_j} \right]$$
 (11)

The turbulence production term  $P_{k\omega}$  is equal to

$$P_{k\omega} = \tau_{ij}^R \frac{\partial u_i}{\partial x_i},\tag{12}$$

and the  $\tau_{ii}^{R}$  is evaluated using the Boussinesq assumption in Eq. (2).

An additional source term  $Q_{SAS}$  is introduced in Eq. (11) for the turbulence dissipation rate to extend these governing equations to SAS canabilities.

$$Q_{SAS} = max \left[ \rho \zeta_2 S^2 \left( \frac{L}{L_{vK}} \right)^2 - F_{SAS} \frac{2\rho k}{\sigma_{\phi}} max \left( \frac{1}{k^2} \frac{\partial k}{\partial x_i} \frac{\partial k}{\partial x_j}, \frac{1}{\omega^2} \frac{\partial \omega}{\partial x_j} \frac{\partial \omega}{\partial x_j} \right), 0 \right]$$
(13)

with the von Kármán length scale  $L_{vK}$  given by

$$L_{\nu K} = \kappa \frac{U'}{|U''|}; \quad U'' = \sqrt{\frac{\partial^2 U_i}{\partial x_k^2} \frac{\partial^2 U_i}{\partial x_j^2}}; \quad U' = \sqrt{2S_{ij}S_{ij}}. \tag{14}$$

#### 2.4. Improved one-equation turbulence model

A modification to the Boussinesq assumption for the SA model is introduced in this work. The enhanced one-equation turbulence model is designated as PK. The extension of the Boussinesq assumption has been used in the URANS simulations with the SAnegRC turbulence model. An effort has been made to address the deficiency in turbulent kinetic energy by introducing a possible variable k specifically tailored for the SA model, designated as  $k_{SA}$ .

Equating production and destruction of the turbulence energy Eq. (10), a simplified equation for k can be derived as follows

$$\beta_c^* k^2 / \nu_t = \tau_{ij}^R \frac{\partial u_i}{\partial x_j} \to k = \frac{1}{\sqrt{\beta_c^*}} \sqrt{\nu_t \tau_{ij}^R \frac{\partial u_i}{\partial x_j}}$$
 (15)

This is consistent with the approach in the QCR model [21]. However, considering the QCR approach, some applications have noted numerical problems with the term  $C_{cr2}\mu_t\sqrt{2S_{mn}^*S_{mn}^*\delta_{ij}}$ , notably in wake regions where  $\mu_t$  is not small [36]. A recommended fix for this problem is to use

vorticity instead of strain in this term, as documented in literature [36]. Consequently, the equation suggested in this work can be expressed as

$$-\rho \overline{u'_{i}u'_{j}} = \tau_{ij}^{R} = 2 \,\mu_{t} \,S_{ij}^{*} - k_{SA} \delta_{ij}, \tag{16}$$

where the SA turbulent kinetic energy is given by

$$k_{SA} = C_k \mu_t \sqrt{2W_{mn}W_{mn}}. (17)$$

The customization of the constant  $C_k$  will be discussed in section 4.4. In this work, the optimal results have been achieved with  $C_k$  being set at 3. This setting is the most effective for the specific conditions and objectives of the study.

#### 3. Computational domain and numerical approach

Fig. 1 shows the ADS-NA2-W1 geometry, a 1:30-scaled version of a generic combat aircraft. A triple-delta wing characterizes this configuration. More details about the wing configuration can be found in reference [22].

The unstructured mesh for investigating the ADS-NA2-W1 geometry comprises approximately 40 million cells. It is constructed with 35 prism layers close to the aircraft, with the first cell layer thickness set such that  $y^+\approx 1$ , and tetrahedral volumes in all other areas. The domain's size is 50 times the characteristic length L, the aircraft's characteristic length in the symmetry plane, as depicted in Fig. 1a. The computational domain is discretized using an unstructured mesh with varying cell sizes. The mesh is most refined near the leading edge, where the inboard and outboard vortex formation begins. The finest cells are approximately 0.001 times the characteristic length. This cell refinement generally tracks the vortices to capture strong gradients and the resolved turbulent fluctuations in the Hi-Fi simulations.

#### 3.1. Analysis of the mesh resolution

Given the challenges and computational demands of conducting grid-resolution studies for LES-type simulations, three additional grid levels were considered for the URANS simulations using the SAnegRC turbulence model to analyze grid effects. This approach balances computational feasibility with the need for meaningful resolution analysis. As the details are extensively covered in the literature [37], they are omitted here to maintain conciseness and avoid redundancy.

To enhance the understanding of grid resolution, this study includes the analysis of essential parameters. These considerations are based on the results of the IDDES model, which necessitates the highest spatial and temporal accuracy level. Furthermore, they are displayed on the windward wing, which exhibits the highest flow velocities and is the primary focus of the analysis conducted in this paper.

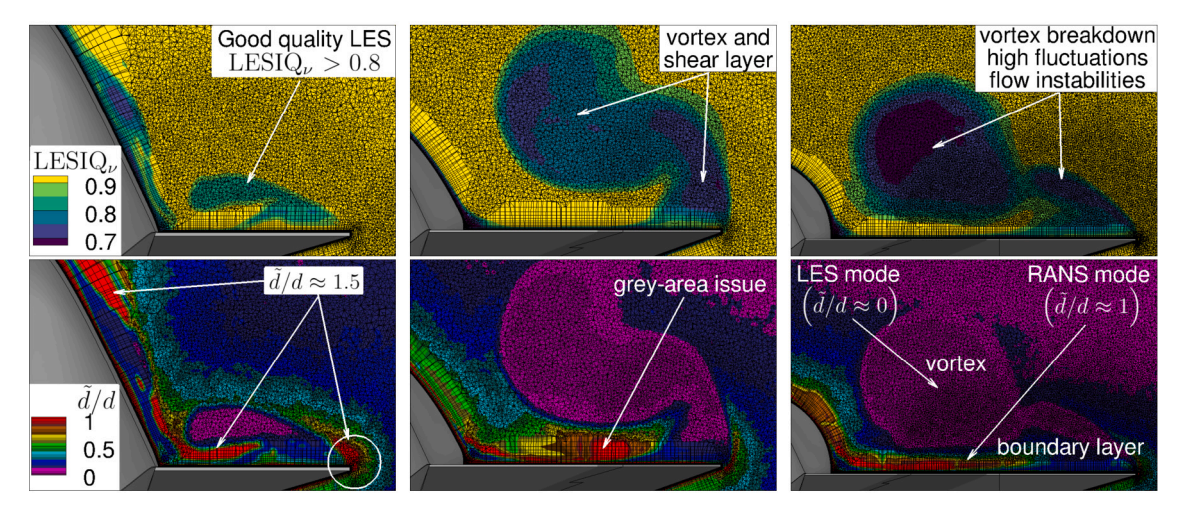


Fig. 2. LES Index of Resolution Quality LESIQ., and mean hybrid length scale over RANS length scale,  $\tilde{d}/d$ , IDDES results at  $\xi = 0.35, 0.55, 0.75$ .

To demonstrate that the current mesh resolution is sufficient to resolve a major part of the turbulence spectrum, the LES Index of Resolution Quality (LESIQ) has been illustrated in Fig. 2. LESIQ $_{\nu}$  is a dimensionless number, ranging between zero and one, calibrated such that it behaves similarly to the ratio of resolved to total turbulent kinetic energy [38]. An index of quality greater than 0.8 is considered perfect for an LES, while a value of 0.95 and higher is associated with DNS quality [39]. Overall, the plots indicate that the spatial resolution within the vortex region is adequate, exhibiting slightly lower, yet still acceptable, values downstream of the vortex breakdown.

Besides, Fig. 2 presents the mean ratio of the hybrid length scale to the RANS length scale, denoted as  $\tilde{d}/d$ . The cell size has been calculated by determining the cube root of the cell volume, represented as  $\Delta = V^{1/3}$ . The ratio  $\tilde{d}/d$  elucidates the transition in the IDDES approach from RANS to LES modes. Thin regions near the wall are entirely governed by the RANS mode, where a ratio approaching unity is expected. Consequently, the vortex development occurs within the LES domain. The transition between the two modes gives rise to the so-called 'grey-area' issue, since the vortex formation initially occurs in near-wall layers modeled by the RANS mode. The challenges associated with the grey area, its impact on the results, and potential mitigation strategies have been extensively analyzed in the literature [16,40].

## 3.2. Numerical setup and solution techniques

Unsteady simulations have been performed using the DLR TAU-Code [28]. An implicit dual-time stepping approach employing a Backward-Euler/LUSGS implicit smoother has been selected. The flux computation has been performed with a central scheme. To stabilize the URANS runs, an artificial dissipation for the central scheme has been added with the matrix dissipation method. However, in scale-resolving (IDDES) and scale-adaptive (SAS) simulations, the artificial dissipation has been reduced to prevent excessive damping of the resolved turbulent structures. A (hybrid) low-dissipation low-dispersion discretization scheme (HLD2) and a vorticity-sensitive sub-grid filter scale, which enhances the development of turbulent structures on anisotropic meshes, have been used for the IDDES runs [41]. For SAS, a low-dissipation discretization scheme (LD) has been used in the SAS runs [41]. More details regarding the numerical approach and the time length series of the simulation to collect the flow field statistics for the different methods can be found in previous work [37,42,43].

In unsteady simulations, it is crucial to account for the time a fluid element takes to traverse the aircraft, which determines the requisite physical or computational time for a reliable solution. The Convective Time Unit (CTU) is computed as  $T=\frac{L}{U_{\infty}}\approx 2\times 10^{-3}$  s, representing 1

CTU, where L denotes the characteristic length, and  $U_{\infty}$  the free-stream velocity.

For URANS simulations, a time step size of  $5 \times 10^{-2}$  CTU has been selected. To mitigate initial transients ten CTUs have been calculated preceding five flow-through times of time-averaging till reaching statistical convergence of the mean flow properties. In Hi-Fi simulations, the maximum allowed time step size was determined to resolve convective transport and accurately capture flow characteristics. The chosen time step size,  $\Delta t = 5 \times 10^{-4}$  CTU, adequately resolves the energy-containing eddies' time scales in the flow of interest, ensuring the convective Courant-Friedrichs-Lewy (CFL) number,  $\frac{U\Delta t}{\Delta}$ , remains below unity in the focus region [26]. The simulations have been initialized with the URANS results to reduce the initial transient. Fifteen CTUs have been computed to reach a statistically steady flow. Subsequently, another fifteen overflows have been considered to calculate statistics of the flow properties.

#### 4. Results and discussion

The flow features a Mach number of  $Ma_{\infty}=0.85$  and a Reynolds number of  $Re_{\infty}=12.53\times 10^6$ . The transonic condition generates a supersonic area over the wing, resulting in different shock waves interacting with the vortices and enhancing vortex breakdown. Fully turbulent conditions are assumed without accounting for transition in the underlying RANS models. URANS and Hi-Fi data have been obtained with side slip angle  $\beta=5^\circ$  and angle of attack  $\alpha=20^\circ$ .

The results of the PK model are initially presented in section 4.1, where they are compared with experimental data in terms of aerodynamic coefficients and surface pressure coefficient. A more thorough analysis of the improvements achieved by the PK model is given in section 4.4. Sections 4.2 and 4.3 offer a comparative assessment of the results from the other approaches, focusing on flow physics and turbulence modeling. These sections are designed to clarify the SA model's shortcomings and disadvantages, thereby elucidating the necessity for the proposed PK modification.

## 4.1. Data comparison: validation of the CFD results

Leading-edge vortices originate from the separated shear-layer at the leading edge, as shown in Fig. 3. As the flow separates over the wing at the leading edge, it rolls up, forming a stable, separation-induced leading-edge vortex. This primary vortex subsequently induces a reattached flow over the wing. Under certain conditions, the spanwise flow beneath this primary vortex separates again, resulting in a counter-rotating secondary vortex outboard of the primary one. Fuse-lage vortices generated from the aircraft apex are also illustrated in

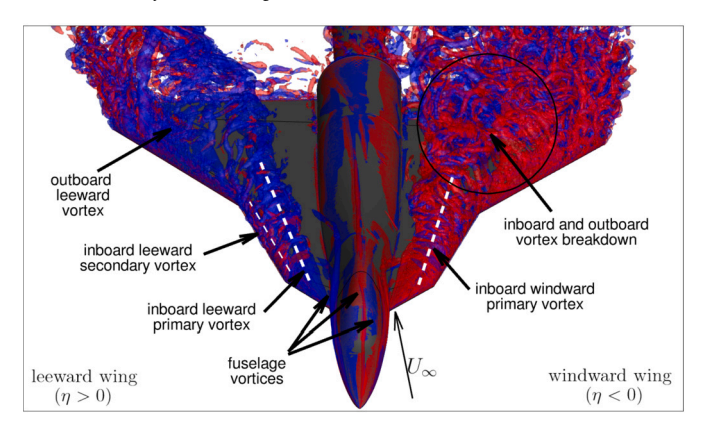


**Fig. 3.** *Q*-criterion instantaneous iso-surface with flood contour by instantaneous normalized helicity  $H_n$ , IDDES results with  $Ma_\infty=0.85$ ,  $Re_\infty=12.53\times10^6$  and  $\beta=5^\circ$ .

Fig. 3. Two distinct vortices are evident on the leeward wing, whereas two more prominent vortices are observed on the windward wing [37]. These vortices are generated in correspondence with the two sweep angles on the first and third leading edge sections. Both windward wing vortices subsequently break down, characterized by an abrupt alteration in flow topology where the flow decelerates and diverges [37]. The onset location of the vortex breakdown is not fixed; it displays buffeting behavior [42]. While a comprehensive understanding of this behavior requires analyzing the instantaneous flow characteristics due to their unsteady effects, this manuscript examines the mean flow features to explore better the turbulence treatments' effects on the RANS results.

#### 4.1.1. Aerodynamic coefficients: analysis of the dependency on AoA

As a primary measure of result accuracy, the rolling and pitching moment coefficient curves are shown in Fig. 4. Experimental data from the literature [22] are juxtaposed with CFD results. These results include URANS from SAnegRC,  $k\omega$ SST, and PK, as well as scale-resolving IDDES and SAS. For a comprehensive view of the predictions, Fig. 4 presents aerodynamic coefficients for various angles of attack. Simulations for different angles of attack have been conducted and discussed in previous works [37,42,43]. Accurately predicting an airplane's aerodynamic coefficients is paramount for designing aircraft stability and controllability. Moments react more sensitively to variations in the flow pattern than force coefficients do. Therefore, the rolling and pitching moment coefficient curves are especially relevant at non-zero side slip angles. These curves exhibit several steep transitions, predominantly attributed to vortex breakdown and re-orientations of the vortices.

The substantial deviation between the results of different approaches at  $\alpha = 20^{\circ}$  primarily results from other predictions of the vortex breakdown on the windward wing. Hi-Fi data enhance the prediction of the aerodynamic coefficients, with the SAS approach appearing to be the most reliable and suitable for the present configurations. Overall, the two-equation  $k\omega$ SST model is superior to the SA one-equation model in predicting the flow field. The factors leading to vortex breakdown are examined to enhance our understanding of the phenomenon and its numerical prediction. The inaccuracies associated with the SA model are analyzed to pinpoint necessary improvements in turbulence modeling. The PK model markedly improves the prediction of aerodynamic coefficients, especially at  $\alpha = 20^{\circ}$ . Furthermore, for other AoAs, the results achieved using the PK model consistently equal or exceed those derived from the original SAnegRC. Thus, it presents a viable alternative to overcome the limitations inherent in the one-equation model. A detailed analysis of its results, including a quantitative assessment of the improvements achieved, will be presented in section 4.4 (see Fig. 15).

#### 4.1.2. Investigation of the suction footprint

When a leading-edge vortex develops over a delta wing's surface, it leads to a region of reduced pressure (or suction) directly beneath it on the wing. This suction footprint contributes significantly to the lift, especially at high angles of attack. Fig. 5 shows the mean surface pressure coefficient on the aircraft. Three different slice planes have been extracted, and the distribution of  $\overline{c_p}$  along the spanwise direction at chordwise positions  $\xi = 0.35, 0.55, 0.75$  is then plotted in Fig. 6.

As evident from Fig. 6, when examining the surface pressure at  $\xi=0.35$ , none of the numerical results fully captures the flow physics over the aircraft. In particular, mispredictions are observed in the fuse-lage vortices' representation at  $\eta\approx|0.1|$  on both wings. Furthermore, not all of them accurately predict the shear-layer separation and the formation of the primary vortex ( $\eta\approx|0.2|$ ). The  $k\omega$ SST and Hi-Fi results are impressive, with the numerical surface pressure closely aligning with experimental data. In contrast, the SAnegRC outcomes are markedly less accurate, failing to approximate the results of the methods above.

On the windward wing at  $\xi=0.55$ , the suction footprint created by the primary inboard vortex is notably consistent when comparing the  $k\omega$ -based results and the SA-based outcomes amongst themselves. The most pronounced differences are seen in the secondary vortex and the flow behavior near the leading edge. The prediction of the secondary vortex is not as accurate as desired; the negative pressure coefficient is either over or underestimated for  $|\eta|>0.35$ . The peak  $\overline{c_p}$  value captured from the secondary vortex indicates that the SAS result overestimates the secondary vortex's strength relative to experimental data. In contrast,  $k\omega$ SST underestimates this effect. Accurately predicting the strength of the secondary vortex is crucial to capture the vortex breakdown phenomenon.

Underestimating the secondary vortex's strength (i.e., when the  $\overline{|c_p|}$  produced by the secondary vortex is too low) results in an upstream prediction of vortex breakdown. Considering the one-equation model, the secondary vortex remains detectable over the windward wing in the SAnegRC and PK results but disappears in the IDDES.

On the leeward wing at  $\xi=0.75$ , the two fully developed primary vortices (inboard and outboard) can still be discerned where the two peaks of  $\overline{c_p}$  are found (at  $\eta\approx0.5$ ). All the numerical results, except for  $k\omega$ SST, tend to slightly overestimate the two suction footprints. The  $k\omega$ SST results, in contrast, do not depict the outboard vortex because a vortex merging occurs. The interaction between the two vortices supports the inboard vortex until they merge. However, this interaction weakens at higher angles of attack, leading the inboard vortex to break down in the wing's aft part, as supported by the literature [42].

The scenario differs on the windward wing. Results indicate that the vortices experience breakdown. The inboard and outboard vortices do not break down simultaneously; the inboard breakdown precedes the outboard one. Whereas the SAnegRC model entirely fails to capture the vortex breakdown, the PK model successfully represents this phenomenon. All other models, except  $k\omega$ SST, predict the breakdown further downstream on the wing compared to experimental data. This difference explains the differing predictions of the aerodynamic coefficients presented in Fig. 4.

#### 4.2. Correlation between vortex breakdown and turbulence modeling

Enhancing a turbulence model requires a deep understanding of the root causes behind its deficiencies. Fig. 7 indicates the flow structure over the aircraft, and by comparing the SAnegRC and  $k\omega$ SST results, the influence of different turbulence models becomes evident. Hi-Fi data have been shown as reference data.

The pivotal distinction between the two methodologies lies in the shock wave's impact emphasized in Fig. 7, which provides a detailed view of the shock-vortex interaction, explicitly highlighting the state of the inboard vortex before and after this interaction. The vortex core undergoes a decrease in velocity and kinetic energy as it moves through

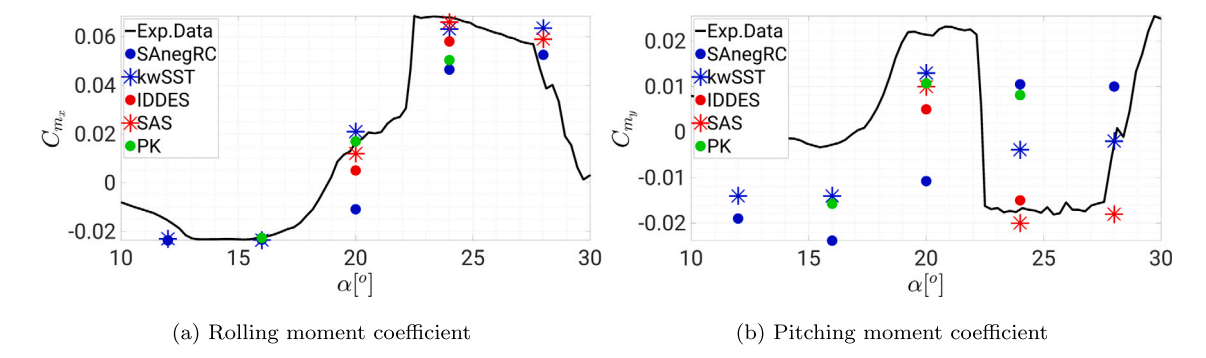


Fig. 4. Experimental and numerical data with  $Ma_{\infty} = 0.85$ ,  $Re_{\infty} = 12.53 \times 10^6$  and  $\beta = 5^{\circ}$ . Hi-Fi results are represented in red, while URANS results are in blue. One-equation and two-equation results are denoted with circle and star markers, respectively.

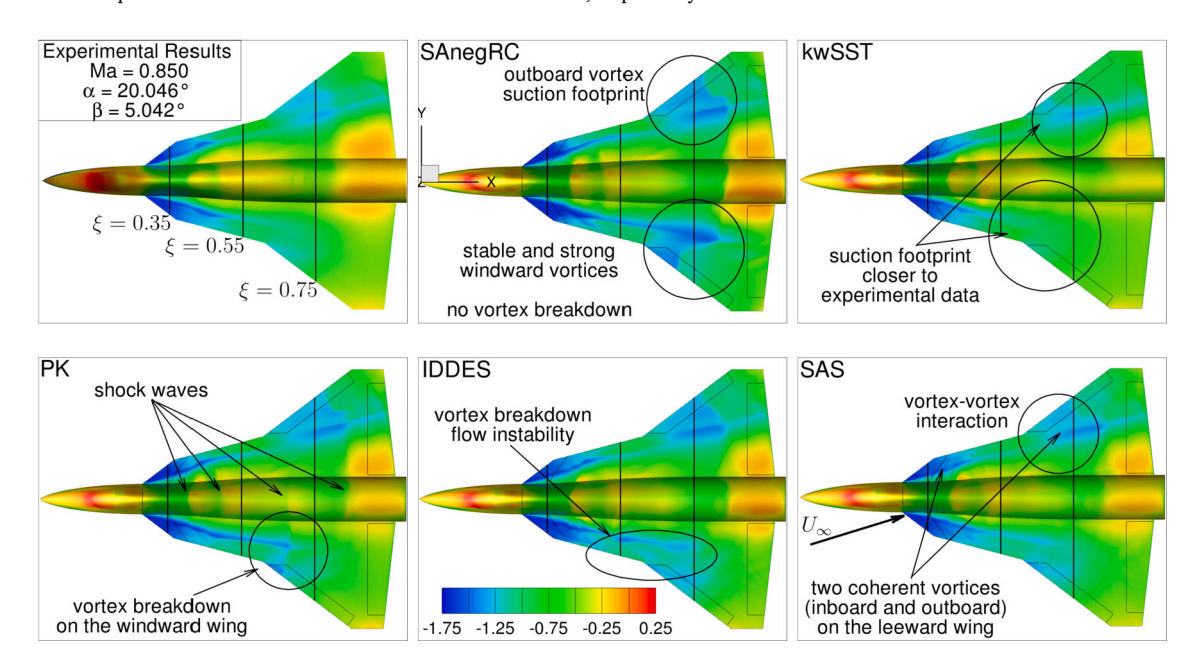


Fig. 5. Mean surface pressure coefficient  $\overline{c_p}$ , experimental and numerical data at  $\beta = 5^{\circ}$  and  $\alpha = 20^{\circ}$ . The black lines show the slice planes.

the shock wave. The interaction between this shock wave and the inboard vortex core is not solely responsible for the observed breakdown. Remarkably, the SAnegRC does not capture this essential occurrence. Hence, it can be concluded that the shock wave does not consistently lead to vortex breakdown. The strength of the vortex is a significant factor [44]. A vortex only breaks down by shock interaction if it's inherently unstable and predisposed to breakdown.

The authors previously proposed a mechanism elucidating the occurrence of vortex breakdown in literature [45]. The core of the inboard vortex is primarily composed of flow from the shear-layer that detaches at the wing apex. Fluid from this separated shear-layer, originating from the leading edge of the apex, forms the core of the inboard vortex and moves along the wing at considerable velocities. As the shear-layer consistently feeds the inboard vortex throughout the wing span, the vortex grows in size. This influx circles the primary core, reinforcing its structure and preserving its cohesiveness. This underlines the importance of accurately capturing separation and turbulence proximate to the apex in delta-wing flow simulations.

Moreover, this phenomenon is supported by the secondary vortex's existence. Once the secondary vortex becomes unsustainable, the boundary layer detaches in the streamwise direction, forming a recirculation zone. Instead of joining the secondary vortex, the fluid transitions into a smaller-scale turbulent motion. This inhibits the shear-layer from coiling into the primary vortex and generates a turbulent flow. The pri-

mary vortex, which loses its source of kinetic energy, becomes more vulnerable.

This theory can be confirmed by analyzing both Fig. 8 and 9. Fig. 8 shows the *x*-vorticity on the windward wing. The velocity inside a leading-edge vortex is higher because the air within the vortex is effectively confined, creating a region of lower pressure at the center of the vortex. This lower pressure at the vortex core leads to higher air velocities swirling around it. This air rotation results in a vorticity concentration within the vortex core.

Fig. 9 depicts the shock-vortex interaction within the vortex core line plane. The unsteady lambda shock, which contributes to the vortex breakdown, is visible. Additionally, Fig. 9 shows the mean friction coefficient  $\overline{c_{f_x}}$  in the *x*-direction, helping to identify the streamwise separation region.

The SAnegRC results show a weaker streamwise separation on the wing before the vortex breakdown. The shear-layer properly feeds the primary vortex. As the consistently positive friction coefficient indicates, the flow remains almost attached to the wing, and the vortex remains stable. Furthermore, the vortex speed increases after the abrupt interaction with the shock. The x-vorticity plot also shows a stable and well-formed secondary vortex. Its formation is delayed, and it does not break down. Conversely, in  $k\omega$ SST, the flow behavior near the apex exhibits significant differences, marked by visible streamwise flow separation, the absence of a coherent secondary vortex, and a negative

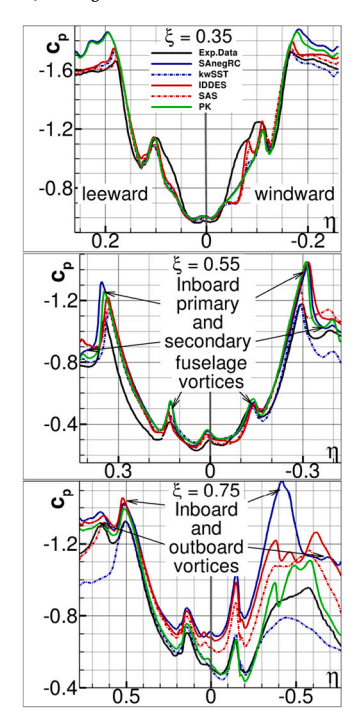


**Fig. 6.** Mean pressure coefficient  $\overline{c_p}$  profiles at chordwise locations  $\xi = 0.35, 0.55, 0.75$ , experimental and numerical data at  $\beta = 5^{\circ}$  and  $\alpha = 20^{\circ}$ .

friction coefficient. This indicates that the leading-edge vortex is already weakened before the interaction. As a result, the vortex in the  $k\omega$ SST results is intrinsically more susceptible to breakdown than that in the SAnegRC results. This difference potentially illuminates the SAnegRC's inability to predict vortex breakdown accurately.

The Hi-Fi data in Fig. 8 confirms and reinforces these analyses, especially when looking at the instantaneous plots. Here, the smaller-scale turbulent motion generated by the secondary vortex breakdown and streamwise separation is visible. It is transported around the primary vortex, and the breakdown then occurs.

#### 4.3. Analysis of the model impact on the turbulence-related quantities

## 4.3.1. Eddy viscosity analysis: turbulence production and destruction

Fig. 10 shows contours of the viscosity ratio  $R_t = \mu_t/\mu$ . The viscosity ratio is compared between the two baseline URANS approaches. The RC correction [24] mitigates the excessive production of eddy viscosity towards the front of the wing. However, in the rear portion of the vortex core, it is inadequate because the SAnegRC model generates markedly elevated levels of eddy viscosity. Instability emerges particularly after the lambda shock location. However, it is counteracted by the viscous damping generated by the SAnegRC model.

The  $k\omega$ SST model features comparable levels of eddy viscosity upstream of the vortex-shock interaction but generally lower levels downstream. Upstream of the vortex breakdown, increased eddy viscosity is primarily observed in the separated shear-layer as it rolls up to form the primary vortex. Following the shock-vortex interaction and the subsequent breakdown, eddy viscosity levels rise due to the vortex's incoherence and the fluid's turbulent motion. This behavior correctly models how turbulent fluctuations destroy the vortex structure. In RANS, regions with large values of  $\mu_t$  typically correspond to vortex motions characterized by high turbulence energy production, which results from intense flow rotation and deformation [16]. Hence, a diminished turbulence level should be observed where the vortex remains coherent. The leading-edge vortex is inherently natural, independent of turbulence, as it does not entail any velocity fluctuations.

Fig. 11 shows the values of both the production and destruction terms from the  $\tilde{v}$  and the k turbulence equations. Specifically, consid-

**Table 1**Source terms of the turbulence equations illustrated in Fig. 11.

	Production Term	Wall Production Term
SA	$P_{\Omega_{SA}} = \left[c_{b_1} \left(1 - f_{t2}\right) \Omega - c_{b_1} f_{t2} \overline{s}\right] \tilde{v}$	$P_{wall_{SA}} = c_{b_1} \overline{s} \tilde{v}$
SAneg	$P_{\Omega_{S,Aneg}} = c_{b_1} \left( 1 - c_{i3} \right) \Omega \tilde{v}$	$P_{wall_{SAnes}} = 0$
SA-RC	$P_{\Omega_{SA-RC}} = f_{r1} P_{\Omega_{SA}}$	$P_{wall_{SA-RC}} = f_{r1} P_{wall_{SA}}$
k-eq	$egin{aligned} P_{\Omega_{SA-RC}} &= f_{r1} P_{\Omega_{SA}} \ P_{k\omega} &=  au_{ij}^R rac{\partial u_i}{\partial x_j} \end{aligned}$	-
	(Wall) Destruction Term	
SA	$\begin{aligned} D_{wall_{SA}} &= \left[ c_{w1} f_w - \frac{c_{b1}}{\kappa^2} f_{t2} \right] \left( \frac{\tilde{v}}{d} \right)^2 \\ D_{wall_{SAREg}} &= -c_{w1} f_w \left( \frac{\tilde{v}}{d} \right)^2 \end{aligned}$	
SAneg	$D_{wall_{SAneg}} = -c_{w1} f_w \left(\frac{\dot{V}}{d}\right)^2$	
SA-RC	$D_{wall_{SA-RC}} = D_{wall_{SA}}$	
k-eq	$D_k = \beta^* \rho \omega k$	

ering the one-equation model, this study provides an analysis of the combination of the SA and SAneg terms written in Eq. (4) and (7) and summarized in Table 1. The rotation correction factor  $f_{r1}$  written in Eq. (8) is plotted for further insight. The SA model does not produce turbulence near the wing's apex or the leading edge where the vortex forms. Furthermore, the production term becomes highly active within the vortex core, particularly after encountering the shock. This accounts for the elevated levels of turbulent viscosity in that region. The model also alternates between positive and negative values, attributable to the RC modification [24]. These fluctuations contribute to the inaccuracies associated with turbulent viscosity.

The wall production term indicates turbulence generation solely at the location of the secondary vortex, which appears stable and well-defined. These observations are juxtaposed with the almost negligible presence of the destruction term, which only partly counterbalances the effects of wall production. While the RC factor adeptly localizes the vortex core, it fails to limit the turbulence production. As mentioned, the SAnegRC model produces too much turbulence in the coherent vortex core, incorrectly stabilizing it. The eddy viscosity can be seen as a quantity that dampens rotation. The more viscous the flow, the slower it rotates. Consequently, the ratio of axial to tangential velocity, defined as the Rossby number, increases, indicating greater stability of the vortex [13].

The  $k\omega$ SST model appropriately predicts turbulence generation in the separation region and partially mitigates turbulence within the vortex. Due to its formulation outlined in section 2.3, it can be observed from the appearance of the destruction term that the presence of k is limited where it is generated and reaches high levels. This indicates that the two-equation model has an inherent ability to self-balance and regulate the turbulent viscosity levels. This capability is less featured by the one-equation model in the context of a vortical flow, necessitating a distinct conceptual approach when addressing such challenging configurations for CFD simulations.

### 4.3.2. Boussinesq assumption and Reynolds stress tensor

A contributing factor to the URANS inaccuracies was believed to be the anisotropy of the Reynolds stress, which the authors addressed in a prior study [43]. The comparison of various modeling strategies illuminated several impacts of the linear Boussinesq hypothesis. Nevertheless, the anisotropy characteristic alone cannot account for the discrepancies in the results produced by the SA and the  $k-\omega$  models, as both rely on the Boussinesq assumption as outlined in Eq. (2). A comparative analysis between the Reynolds stress from SAnegRC and  $k\omega$ SST underlines the impact of turbulence or, even better, the effect of not explicitly having the turbulence kinetic energy k in SA. Hi-Fi data have also been provided as a reference.

The Reynolds stresses  $au_{ij}^R$  represent the intensity of the turbulent fluctuations along the three directions and their covariance. The Reynolds stresses are computed considering the resolved and the modeled parts,  $au_{ij}^R = au_{ij}^{mod} + au_{ij}^{res}$ . Considering the mean flow field, the modeled Reynolds stresses  $au_{ij}^{mod}$  are derived from the Boussinesq assump-

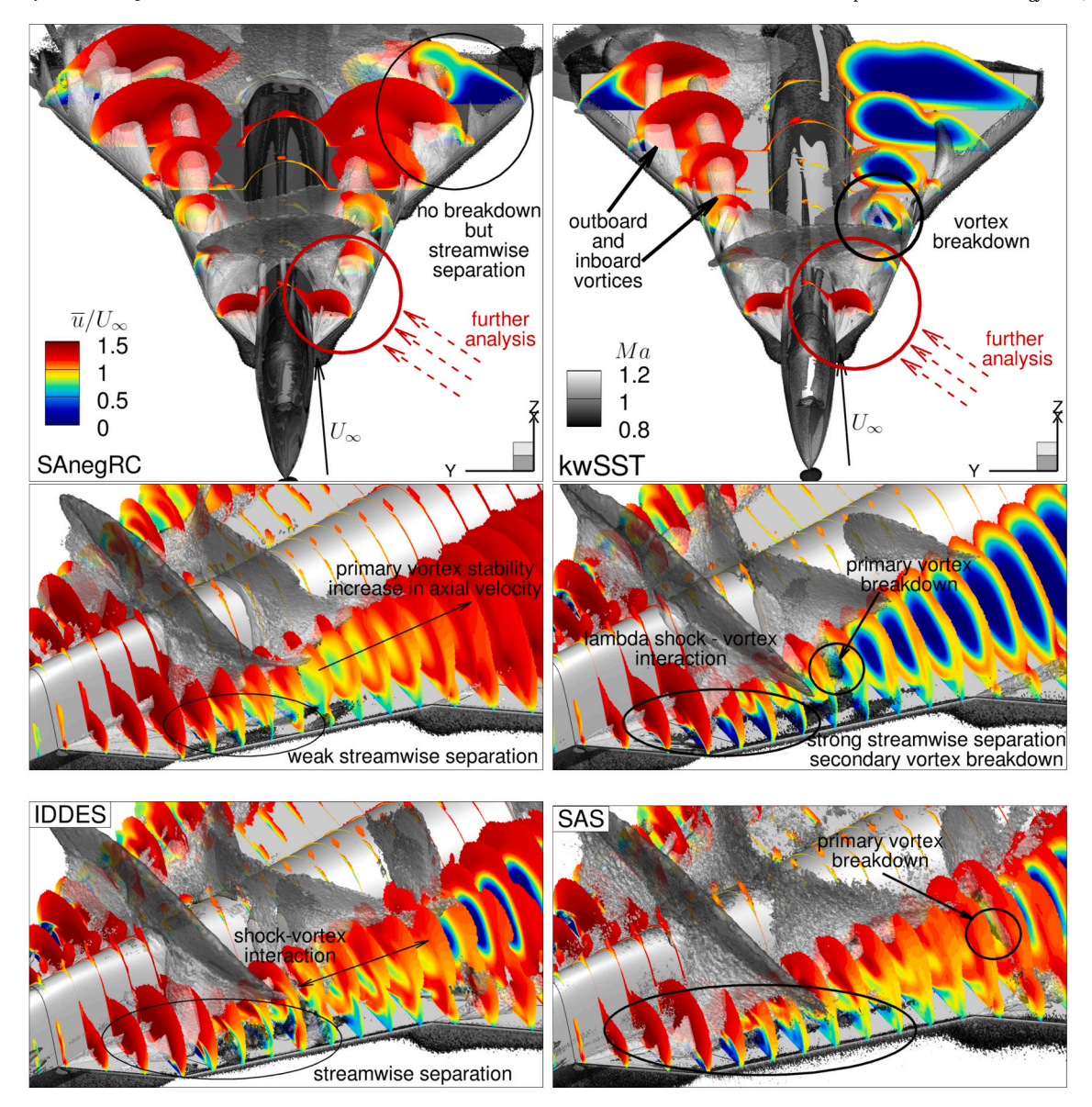


Fig. 7. Iso-surfaces from streamwise pressure gradient and Q-criterion colored by Mach number Ma, and slice planes showing the normalized x-velocity  $\overline{u}/U_{\infty}$ .

tion in Eq. (2). Statistics of the resolved fluctuations have been collected to calculate the resolved Reynolds stresses  $\tau_{ij}^{res} = -\overline{u_i'}u_j'$ . Fig. 12 shows two normal components of the normalized Reynolds stress tensor  $\tau_{ii} = \tau_{ii}^R/(\overline{\rho}U_\infty^2)$  on the windward wing. They have been normalized by free-stream velocity and local mean density. They then represent the variance of the velocity components.

The SAnegRC results display non-physical positive values of  $\tau_{ii}$ , which must be negative due to the negative sign before the squared velocity fluctuations. This characteristic is absent in the  $k\omega$ SST results due to including the turbulent kinetic energy k, as written in Eq. (2) and illustrated in Fig. 13.

By definition, k is assumed zero in the one-equation model, and this presumption yields incorrect values for the normal Reynolds stresses. This leads to the hypothesis that the isotropic component of the Boussinesq assumption, given as  $2/3\rho k\delta_{ij}$ , is crucial for such CFD investigations and needs to be incorporated into one-equation models. Indeed, there's a noticeable difference in the magnitude of the Reynolds stresses between the two methodologies. An alternative representation for k is necessary to introduce the isotropic term into the Boussinesq hypothesis for one-equation turbulence models.

Furthermore,  $\tau_{11}$  illustrates the turbulent nature of the turbulent shear-layer, especially evident in the  $k\omega$  findings. Streamwise turbulent motion is more pronounced in the separated boundary layer and intensifies after the vortex breakdown, transporting the turbulence kinetic energy downstream. Even upstream of the breakdown location, velocity fluctuations are mildly present within the leading-edge vortex core. As Menke and Gursul [46] demonstrated, these fluctuations result from a random displacement of the vortex core.

In the SAnegRC results,  $\tau_{11}$  becomes markedly negative downstream of the shock-vortex interaction location, underlining the non-stationarity of the phenomena. The averaged Navier-Stokes equations only feature the divergence of the Reynolds stress tensor. The turbulence effects in the averaged momentum equation can be depicted by the body force  $f = \nabla \times \tau^R_{ij}$ , as mentioned in section 2.1. This implies that a negative gradient of the Reynolds stress tensor yields an opposing force that slows the flow field over the aircraft and vice-versa. This flow's behavior is evident right after the shock but does not lead to a breakdown in the SAnegRC results.

On the other hand, as previously highlighted, the turbulence model inaccurately reinforces a coherent vortex. The positive gradient of Reynolds stresses further seems to corroborate this interpretation.  $\tau_{22}$ 

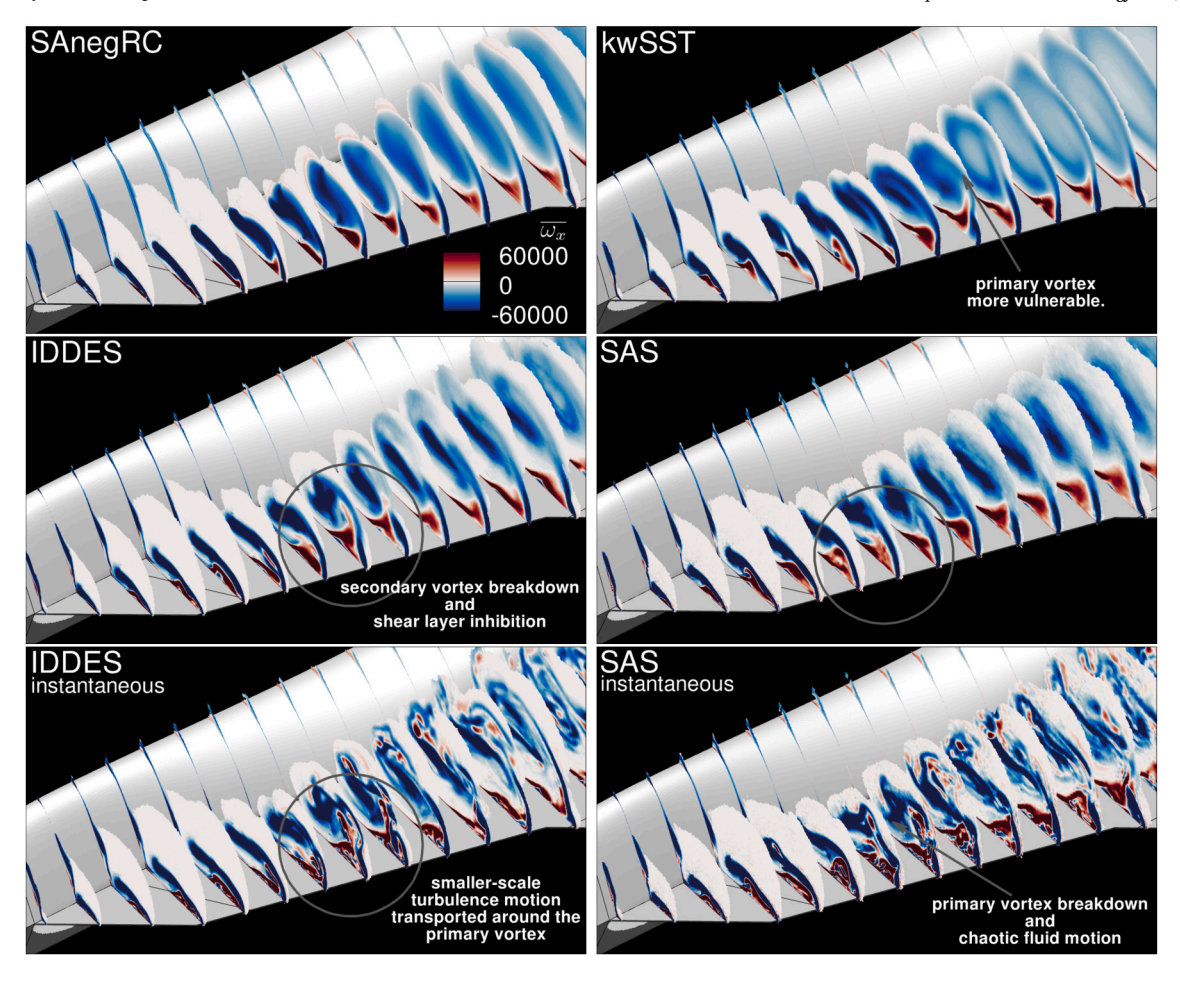


Fig. 8. Mean and instantaneous x-vorticity  $\omega_x$ , URANS, and Hi-Fi results.

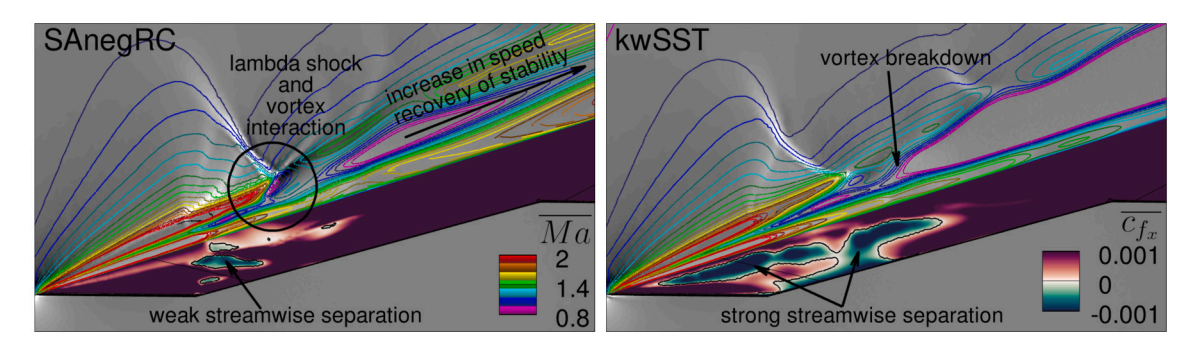
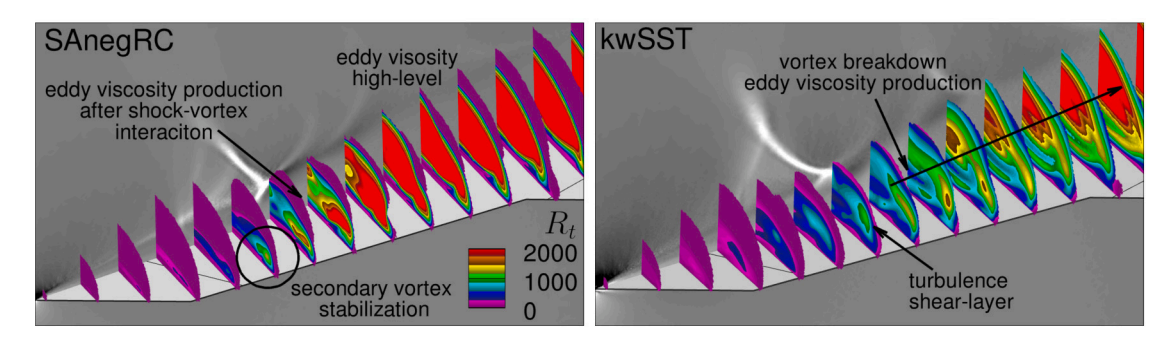


Fig. 9. x-pressure gradient contour field with Mach number contour lines and mean x-direction friction coefficient. Black lines: zero mean friction coefficient.



**Fig. 10.** Viscosity ratio  $R_t$  in the windward inboard vortex.

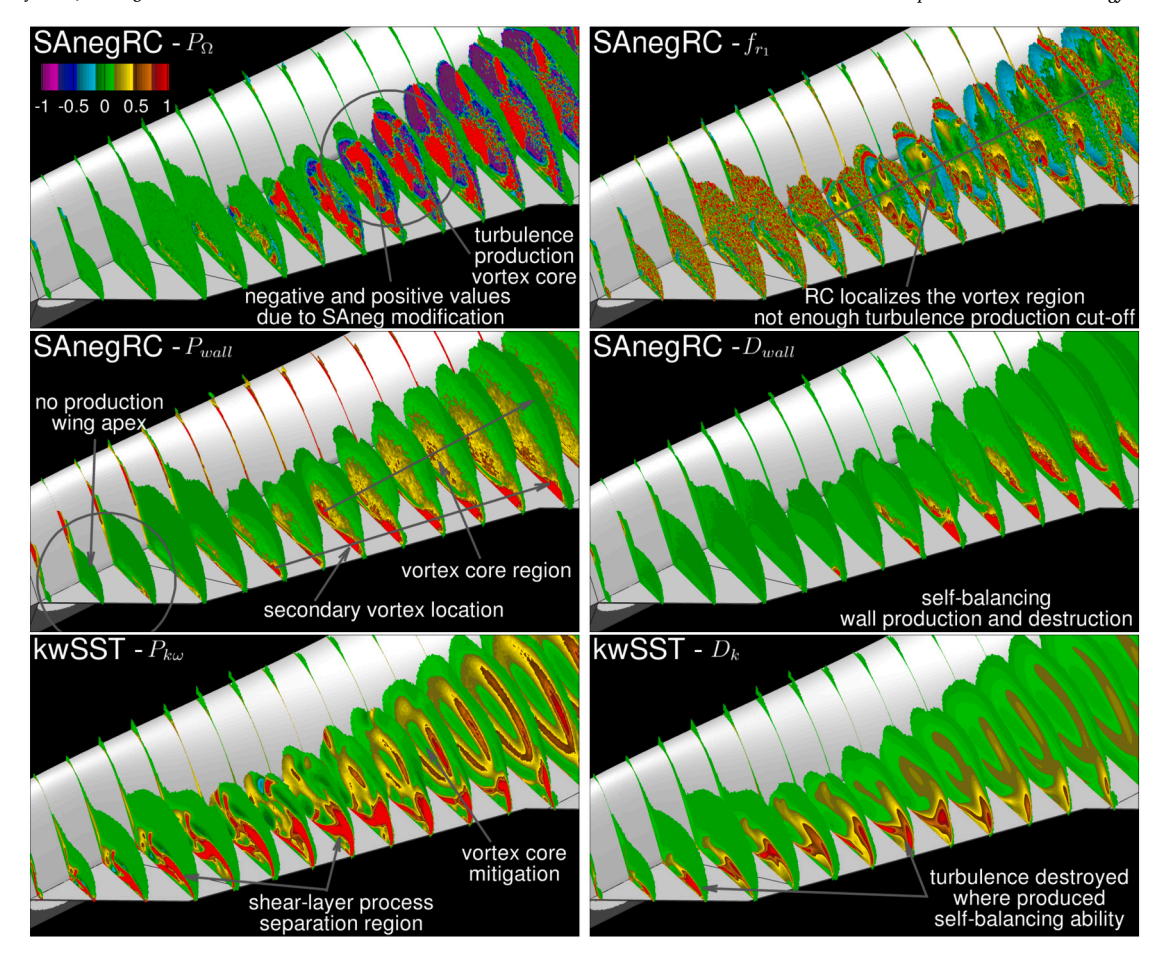


Fig. 11. Source terms of the turbulence equations written in Table 1. All the values have been normalized.

indicates that the fluctuations are generated as the flow departs from the leading edge, and it is the primary source of the turbulence kinetic energy within the vortex core. Compared to the  $k\omega$ SST results,  $\tau_{22}$  appears almost negligible in the SAnegRC findings.

## 4.4. Improved one-equation results

As previously outlined in section 2.4, the constant  $C_k$  required customization based on the findings of k (see Fig. 13). Initially, an estimate of  $C_k$  was derived from the QCR model and refined using the  $k\omega$ SST results through the inversion of Eq. (17), as depicted in Fig. 14. Several values of  $C_k$  have then been tested to find the best value and provide insights into the proposed modification.

To facilitate a quantitative comparison between the simulation results and experimental data, the relative deviation of the aerodynamic coefficient introduced in section 4.1 has been computed for  $\alpha=20^\circ$  and depicted in Fig. 15. The results achieved with  $C_k$  equals to  $C_{cr2}=2.5$ , originally from the QCR method [36], 3.0, and  $1/\sqrt{\beta_c^*}=3.\overline{3}$  from the Bradshaw hypothesis [47], are compared with the CFD results previously discussed.

The QCR results, presented by the authors in a prior work [43], are also included in this plot. The new model also exhibits greater stability and robustness than the QCR, demonstrating a faster convergence rate. The coefficient  $C_k$  plays a crucial role and must be accurately calibrated to predict the precise location of the vortex breakdown. As the value of  $C_k$  increases, the breakdown moves further up the wing, eventually aligning with the position predicted by experimental observations. At this juncture, the pitching coefficient  $C_{m_y}$  becomes less sensitive to variations in  $C_k$ .

Conversely, the rolling moment  $C_{m_x}$  continues to undergo substantial changes with alterations in  $C_k$  because the latter exerts a more significant influence on the leeward wing. The PK model enhances the prediction of aerodynamic coefficients, resulting in a notable reduction of deviations compared to SAnegRC. As mentioned above, the optimal results were attained with  $C_k$  set to 3, and a detailed analysis follows.

Fig. 16 illustrates the predicted flow phenomena above the aircraft using the PK turbulence model with  $C_k = 3$ . The enhanced model successfully captures a more pronounced streamwise separation near the leading edge and the subsequent vortex breakdown over the windward wing, albeit at a more downstream location. The PK model demonstrates superior prediction and instability of the secondary vortex. This improvement manifests in a more pronounced streamwise separation, as observed in the  $\overline{c_{f_s}}$  plot. A more accurate depiction of the lambda shock shape is achieved, contributing to a more reliable prediction of the shock-vortex interaction process. The Mach contour lines align more closely with those predicted by the  $k\omega$ SST model, although the vortex breakdown occurs further downstream. Whereas the  $k\omega$ SST model captures anticipated vortex breakdown on the wing compared to the experimental results, the PK model appears to capture a more accurate position, similar to that obtained from Hi-Fi data. Fig. 17 shows the turbulence-related quantities of the PK results.

The PK model attenuates turbulence production in the vortex core, particularly close to the leading edge where the shear-layer separates, and the viscosity ratio values align more closely with those observed in the  $k\omega$ SST model. The k modeling accurately depicts the separation of the shear-layer at the leading edge, the development of vortices, and the streamwise separation close to the wing apex. The secondary vortex breaks down, and the chaotic motion is visible. The new extension of Boussinesq's assumption yields an accurate prediction of the

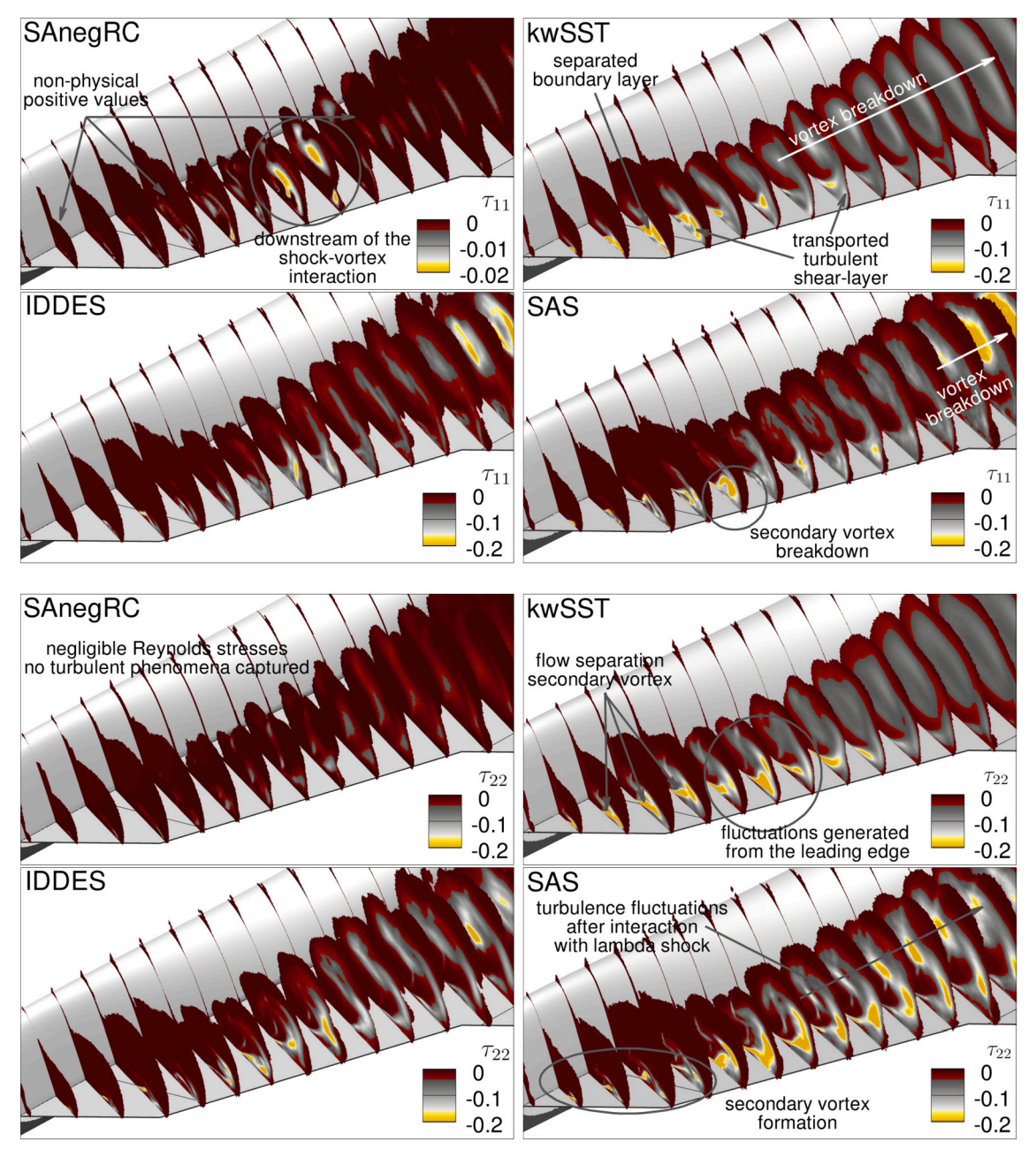


**Fig. 12.** RANS and Hi-Fi results, normalized specific Reynolds stresses  $\tau_{ii}$ .

Reynolds normal stresses, which are no longer erroneously positive. The PK model is a promising way to improve the one-equation RANS-predicted flow physics around a delta wing in transonic conditions. To enhance this extension further, the coefficient  $C_k$  could be derived through optimization processes involving the formulation of a function that varies within the flow field.

## 5. Conclusion and outlook

This study has presented results from five distinct simulations of the transonic flow around a generic triple-delta wing aircraft. They include URANS based on the Spalart-Allmaras with negative turbulent viscosity corrections and rotation/curvature corrections, URANS based on the Menter  $k\omega$ SST model, URANS based on the PK model, IDDES, and SAS. The PK model represents a novel and straightforward extension to the Boussinesq assumption, initially introduced for the SAnegRC turbulence

model, aimed at replicating the turbulent kinetic energy effect observed in the  $k\omega$ SST results.

The accuracy of the integral moment coefficients is mainly related to the prediction accuracy of the vortex breakdown. High-fidelity simulations enhance the prediction of the aerodynamic coefficients. Whereas the SAnegRC model entirely fails to capture the vortex breakdown, the PK model successfully represents this phenomenon. The PK method significantly improves the prediction of aerodynamic coefficients, leading to a substantial reduction in deviations compared to SAnegRC results.

The primary vortex only breaks down due to shock interaction if it is inherently unstable and predisposed to breakdown. The inconsistent predictions of the vortex breakdown onset location can be attributed to the upstream conditions of the vortex, with the shear-layer separation near the wing apex and the secondary vortex formation being especially noteworthy. The SAnegRC results show a weaker streamwise separation on the wing upstream of the vortex breakdown. Conversely, the streamwise flow separation is markedly visible near the apex of the

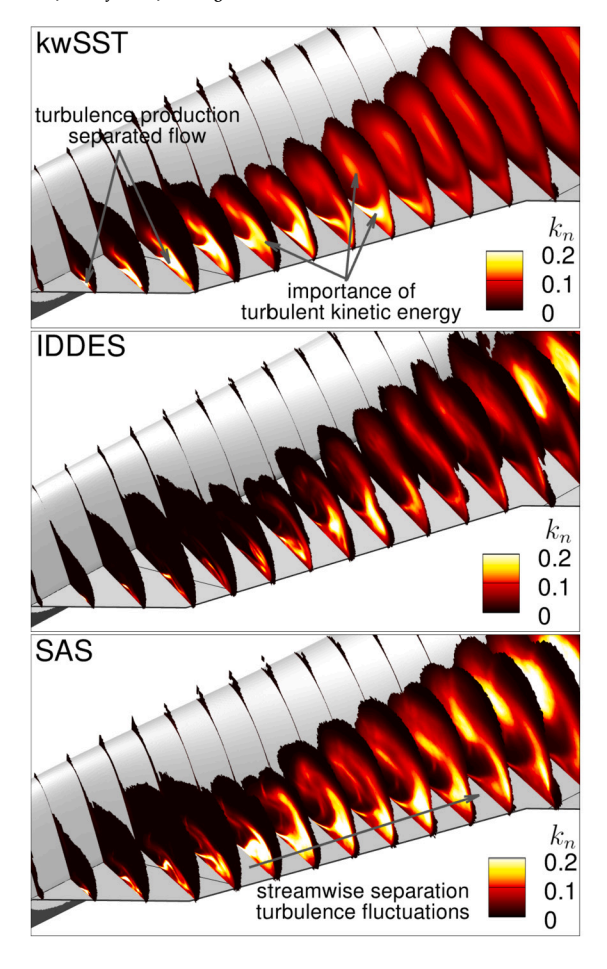


Fig. 13. Normalized turbulent kinetic energy.

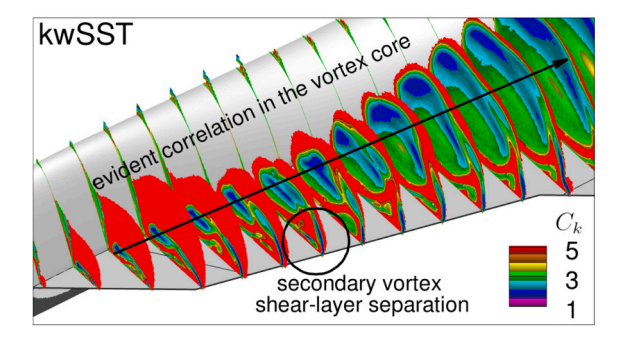


Fig. 14. Correlation between vorticity magnitude and turbulent kinetic energy.

wing in  $k\omega$ SST results, and no coherent secondary vortex is present. The shear-layer emanating from the leading edge does not correctly feed the primary vortex. The primary vortex predicted by  $k\omega$ SST is intrinsically more susceptible to breakdown than that from SAnegRC. The PK model effectively captures a more pronounced streamwise separation near the leading edge. A more accurate depiction of the lambda shock shape is achieved, enhancing the reliability of predicting the shock-vortex interaction process.

The SAnegRC model does not produce turbulence near the wing apex or the leading edge where the vortex forms. Furthermore, the production term becomes highly active within the vortex core, particularly after encountering the shock. This accounts for the elevated levels of turbulent viscosity within the vortex core. The  $k\omega$ SST model appropriately predicts turbulence generation in the separation region and partially succeeds in mitigating the production within the vortex. The PK model aligns viscosity ratio values more closely with those ob-

served in the  $k\omega$ SST model. In the one-equation model, k is assumed to be zero, yielding non-physical values for the normal Reynolds stresses. The Boussinesq assumption's isotropic component is crucial in the investigated case and has been incorporated into the one-equation PK model.

The PK model appears promising for enhancing the one-equation RANS-predicted flow physics around a delta wing in transonic conditions. Additional research and analysis are necessary to optimize the  $k_{SA}$  function. This refinement is crucial for enhancing the model's applicability and accuracy in diverse flow conditions. The present study serves as a basis and motivation for developing a modified constitutive relation for specific applications in future work. They will focus on developing a one-equation turbulence model specifically adapted for accurately simulating leading-edge vortices. Future work will include various geometries and Mach numbers, contingent upon the availability of experimental data. The PK model may also introduce unintended side effects or necessitate the recalibration of some SA coefficients. Consequently, a series of canonical test cases (e.g., flat plate, 2D airfoil, 2D hump) will be conducted to perform preliminary assessments using both compressible and incompressible solvers.

### CRediT authorship contribution statement

**Tony Di Fabbio:** Writing – original draft, Methodology, Investigation, Conceptualization. **Karthick Rajkumar:** Writing – review & editing, Visualization. **Eike Tangermann:** Writing – review & editing, Resources, Funding acquisition. **Markus Klein:** Supervision, Funding acquisition.

#### **Declaration of competing interest**

The authors declare the following financial interests/personal relationships which may be considered as potential competing interests:

Tony Di Fabbio reports financial support was provided by Airbus Defence and Space GmbH. If there are other authors, they declare that they have no known competing financial interests or personal relationships that could have appeared to influence the work reported in this paper.

## Data availability

Data will be made available on request.

#### Declaration of AI-assisted technologies in the writing process

During the preparation of this work the author(s) used ChatGPT OpenAI in order to improve language and readability. After using this tool/service, the author(s) reviewed and edited the content as needed and take(s) full responsibility for the content of the publication.

## Acknowledgements

The financial support for this research provided by Airbus Defence and Space as part of the project "Efficient Turbulence Modelling for Vortical Flows from Swept Leading Edges" is deeply appreciated. We also value the assistance with the experimental data of the ADS-NA2-W1 aircraft. Our gratitude extends to the German Aerospace Center (DLR) for supplying the DLR TAU-Code, which was instrumental in the numerical analysis of this study. The contribution of Ennova Technologies Inc. in providing meshing software is also earnestly acknowledged. Lastly, we thank the Gauss Centre for Supercomputing for their generous allocation of computing time on the GCS Supercomputer SuperMUC at the Leibniz Supercomputing Center under the account number pn29xa.

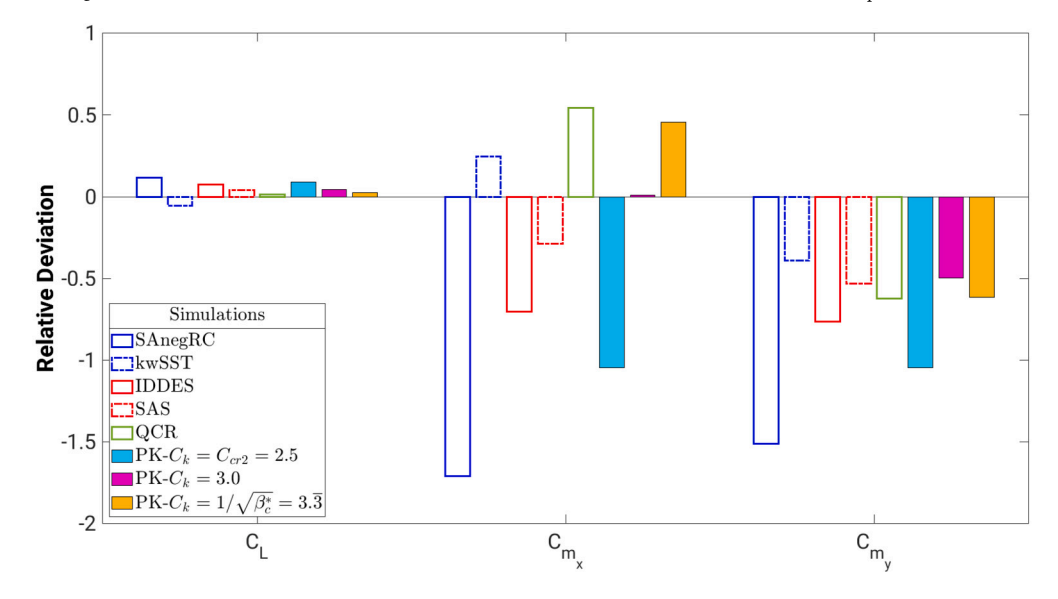


**Fig. 15.** Absolute and relative deviation of the aerodynamic coefficients at  $\alpha = 20^{\circ}$ .

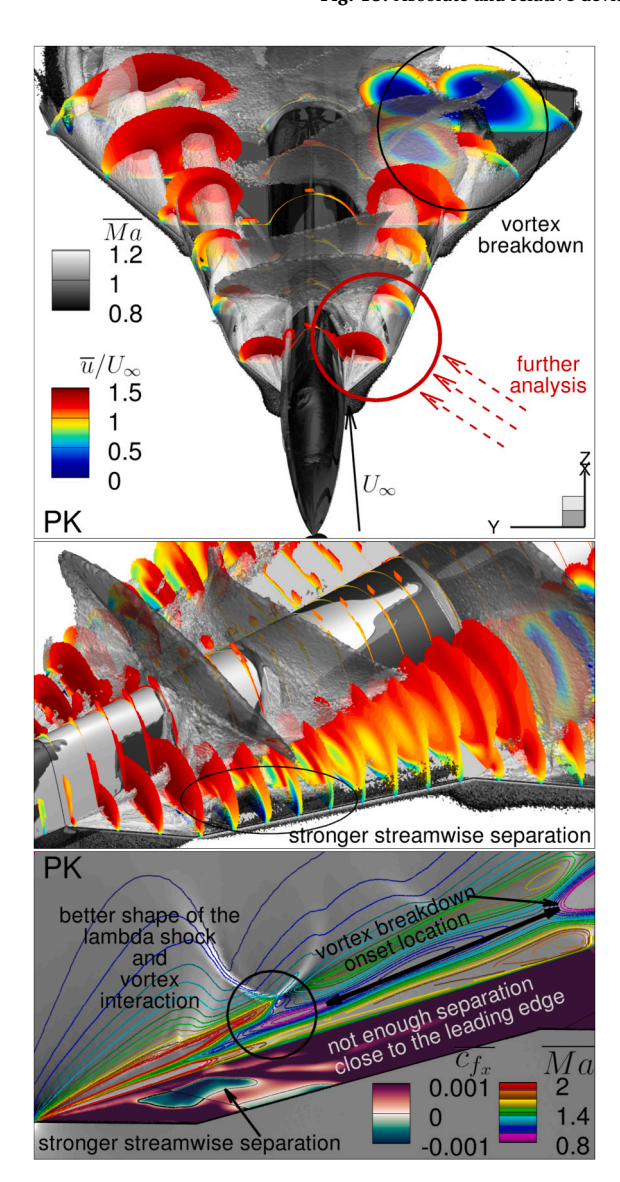


Fig. 16. PK model results: vortices, vortex-shock interaction stream-wise separation and vortex breakdown.

#### Appendix A. Spalart-Allmaras one-equation turbulence model

Devised initially focusing on aerodynamic flows, the model integrates various components in its transport equation to encapsulate the balancing physical phenomena within a wall-bounded turbulent flow. Its design goals included numerical stability, local validity, and Galilean invariance. The local approach of the model allows for the computation of  $v_t$  at individual points independently of the domain's other points, significantly benefiting its application to unstructured grid frameworks. The Spalart-Allmaras model is robust in handling both wall and freestream boundary conditions. Its convergence rate, stability, and accuracy efficiency have been validated through numerous applications, especially in scenarios involving attached or mildly separated flows, making it a popular choice in contemporary numerical studies.

Free Shear Flows. The material derivative of  $v_t$  on the left-hand side of the equation finds a balance with the right-hand side terms, incrementally added to an initial formulation for free-shear flows, each signifying singular additional phenomena. The right-hand side principally includes production and a diffusion term in a free-shear flow scenario. A scalar norm S, essential for evaluating the deformation tensor  $\partial u_i/\partial x_j$ , must accompany  $v_t$ . This norm is invariant, and in the original formulation, the vorticity norm  $\Omega$  was used mainly because, in the targeted applications, areas with dominant vorticity usually exhibit significant turbulence. However, other metrics like strain rate or the complete tensor norm could be equally effective. For consistency with the original formulation,  $\Omega$  will be represented as S. Thus, the baseline production term becomes  $c_{b1}Sv_t$ .

The diffusion term is constructed on the spatial derivative of  $v_t$  and employs the operator  $\nabla \cdot \left( (v_t/\sigma) \nabla v_t \right)$ , where  $\sigma$  is the Prandtl number. Notably, this term lacks conservativeness, a trait commonly accepted in turbulence modeling, albeit not always preferable. The diffusion term is then modified to  $(1/\sigma) \left[ \nabla \cdot \left( v_t \nabla v_t \right) + c_{b2} (\nabla v_t)^2 \right]$ , granting a conservative nature to the  $v_t^{1+c_{b2}}$ . Therefore, the model considered appropriate for free shear flow scenarios is expressed as

$$\frac{\partial v_t}{\partial t} + u_j \frac{\partial v_t}{\partial x_j} = c_{b1} S v_t + \frac{1}{\sigma} \left[ \frac{\partial}{\partial x_j} \left( v_t \frac{\partial v_t}{\partial x_i} \right) + c_{b2} \frac{\partial v_t}{\partial x_i} \frac{\partial v_t}{\partial x_i} \right]. \tag{A.1}$$

**Wall Destruction.** Incorporating wall effects destroys the Reynolds shear stress, dependent on the wall distance d. The term  $-c_{w1}\left(v_t/d\right)^2$  is integrated for this purpose. This term becomes negligible in free-shear flows where the distance approaches infinity, ensuring it does not modify the previous calibration suitable for free-shear flows. Applications demonstrate accurate replication of the log layer in boundary layers

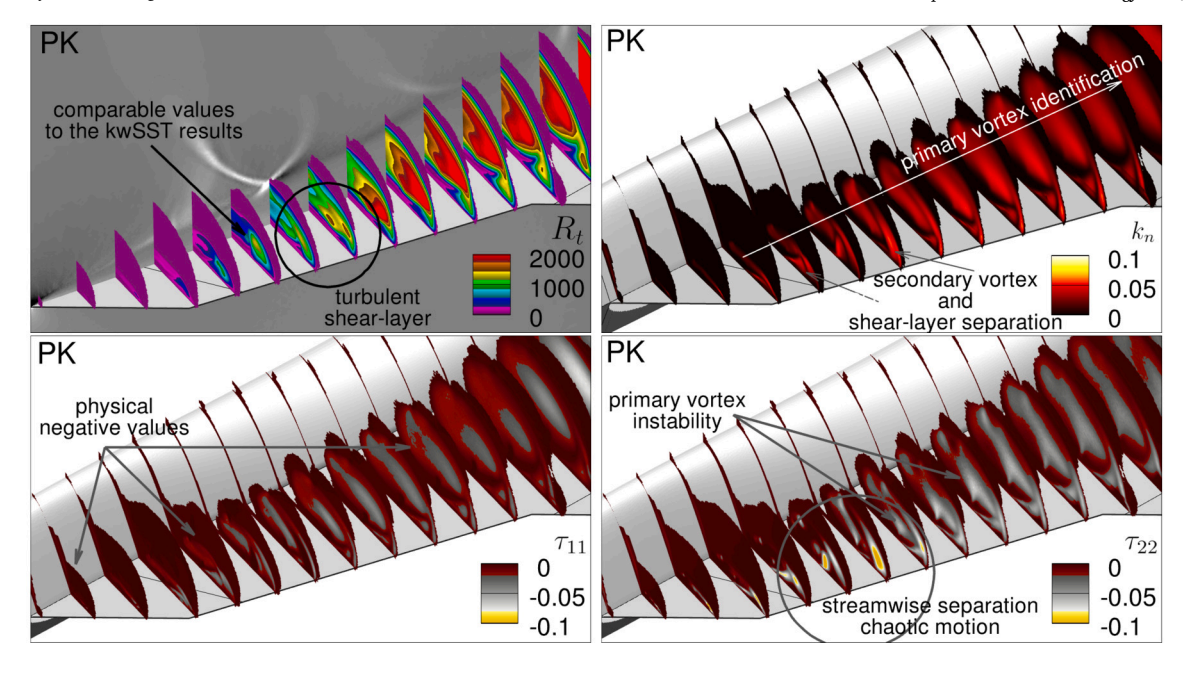


Fig. 17. PK model results: viscosity ratio; normalized turbulent kinetic energy and normalized normal Reynolds stresses.

but tend to underestimate skin friction coefficients over flat plate flows. To rectify this, a non-dimensional smoothing function  $f_{\omega}$ , based on dimensionless mixing length,

$$r = \frac{v_t}{S\kappa^2 d^2},\tag{A.2}$$

is applied to the destruction factor. The function is defined as follows

$$f_{\omega}(r) = g \left[ \frac{1 + c_{\omega 3}^6}{g^6 + c_{\omega 3}^6} \right]^{\frac{1}{6}}, \text{ where } g = r + c_{\omega 2}(r^6 - r)$$
 (A.3)

Spalart and Allmaras [33] also considered the buffer and viscous sublayer modeling, introducing a modified eddy viscosity  $\tilde{v}$ , equivalent to  $v_t$  except in the viscous region. A smoothing function  $f_{v1}$  is applied, equalizing eddy viscosity to  $\kappa y u_{\tau}$  in both the log and buffer layers, as follows:

$$v_t = \tilde{v} f_{v1}$$
, where  $f_{v1} = \frac{\chi^3}{\chi^3 + c_{v1}^3}$  with  $\chi = \frac{\tilde{v}}{v}$ . (A.4)

The production term requires another smoothing function  $f_{v2}$ , ensuring appropriate behavior across different boundary layer stages. Consequently, S is replaced by  $\tilde{S}$  as follows

$$\tilde{S} = S + \frac{\tilde{v}}{\kappa^2 d^2} f_{v2}, \text{ with } f_{v2} = 1 - \frac{\chi}{1 + \chi f_{v1}},$$
 (A.5)

to maintain log-layer dependence as  $\tilde{S} = u_{\tau}/(\kappa y)$ .

The final formulation step of the turbulence model considers laminar and transition regions. However, the transition-triggering term is omitted here, as our research focuses on fully turbulent cases for which the model is predominantly utilized. The addition for laminar regions ensures  $\tilde{v}=0$  as a stable solution of the model equation, assuming  $\tilde{v}$  should be at most of the order of v in laminar conditions. The production term is thus modified with  $1-f_{12}$ , and the destruction term is accordingly balanced. The function  $f_{12}$  is formulated as follows

$$f_{t2} = c_{t3} \exp(-c_{t4} \chi^2).$$
 (A.6)

In the end, after all the previous steps, the model's equation for the modified eddy viscosity,  $\tilde{v}$ , is presented in its incompressible form as follows

$$\frac{\partial \tilde{v}}{\partial t} + u_j \frac{\partial \tilde{v}}{\partial x_i} = c_{b1} \left( 1 - f_{t2} \right) \tilde{S} \tilde{v} - \left[ c_{w1} f_w - \frac{c_{b1}}{\kappa^2} f_{t2} \right] \left( \frac{\tilde{v}}{d} \right)^2 \tag{A.7}$$

$$+\frac{1}{\sigma} \left[ \frac{\partial}{\partial x_i} \left( (\nu + \tilde{\nu}) \frac{\partial \tilde{\nu}}{\partial x_i} \right) + c_{b2} \frac{\partial \tilde{\nu}}{\partial x_i} \frac{\partial \tilde{\nu}}{\partial x_i} \right]. \tag{A.8}$$

with

$$\begin{split} c_{b1} &= 0.1355, \quad \sigma = \frac{2}{3}, \quad c_{b2} = 0.622, \quad \kappa = 0.41, \\ c_{w1} &= \frac{c_{b1}}{\kappa^2} + \frac{1 + c_{b2}}{\sigma}, \quad c_{w2} = 0.3, \quad c_{w3} = 2.0, \\ c_{v1} &= 7.1, \quad c_{t3} = 1.1, \quad c_{t4} = 0.5. \end{split} \tag{A.9}$$

This model has gained widespread usage in external aerodynamic flow studies, particularly in attached flow conditions, where it exhibits optimal performance in terms of accuracy due to its formulation and calibration procedure. It demonstrates significant numerical stability and robustness, with minimal sensitivity or critical outcomes relative to initial and free-stream conditions. A typical free-stream value for  $v_t$  is significantly lower than  $v_t$ , aiding in resolving potential solver issues where rounding errors or divisions by  $\tilde{v}$  are involved in the model's implementation.

#### References

- [1] S.M. Hitzel, A. Winkler, A. Hövelmann, Vortex flow aerodynamic challenges in the design space for future fighter aircraft, in: New Results in Numerical and Experimental Fluid Mechanics XII: Contributions to the 21st STAB/DGLR Symposium, Darmstadt, Germany, 2018, Springer, 2020, pp. 297–306.
- [2] R. Cummings, A. Schütte, S. Schmidt, D. Hummel, E. Milanov, R. Konrath, Z. Zlatev, T. Loeser, C. Simonsen, M. Oehlke, G. Anne, D. Otter, J.-F. Roy, S. Hitzel, D. Rohle, D. Pallek, E. Roosenboom, A. Schröder, K. Petterson, S. Perkins, Assessment of stability and control prediction methods for nato air and sea vehicles (04 2012), https://doi.org/10.14339/RTO-TR-AVT-161.
- [3] M. Escudier, Vortex breakdown: observations and explanations, Prog. Aerosp. Sci. 25 (2) (1988) 189–229, https://doi.org/10.1016/0376-0421(88)90007-3.
- [4] A. Schütte, D. Hummel, S.M. Hitzel, Flow physics analyses of a generic unmanned combat aerial vehicle configuration, J. Aircr. 49 (6) (2012) 1638–1651.
- [5] L.A. Schiavetta, O.J. Boelens, S. Crippa, R.M. Cummings, W. Fritz, K.J. Badcock, Shock effects on delta wing vortex breakdown, J. Aircr. 46 (3) (2009) 903–914.
- [6] A. Schütte, O.J. Boelens, M. Oehlke, A. Jirásek, T. Loeser, Prediction of the flow around the x-31 aircraft using three different cfd methods, Aerosp. Sci. Technol. 20 (1) (2012) 21–37.
- [7] R.M. Cummings, J.R. Forsythe, S.A. Morton, K.D. Squires, Computational challenges in high angle of attack flow prediction, Prog. Aerosp. Sci. 39 (5) (2003) 369–384.

- [8] R.M. Cummings, A. Schütte, Detached-eddy simulation of the vortical flow field about the vfe-2 delta wing, Aerosp. Sci. Technol. 24 (1) (2013) 66–76.
- [9] M. Werner, A. Schütte, S. Weiss, Turbulence Model Effects on the Prediction of Transonic Vortex Interaction on a Multi-Swept Delta Wing, AIAA SCITECH Forum, San Diego, CA, 2022.
- [10] S. Crippa, A. Rizzi Steady, Subsonic CFD analysis of the VFE-2 configuration and comparison to wind tunnel data, https://doi.org/10.2514/6.2008-397, 2008.
- [11] D. Hummel, Review of the second international vortex flow experiment (VFE-2), https://doi.org/10.2514/6.2008-377, 2008.
- [12] W. Fritz, R. Cummings, What was learned from the numerical simulations for the vfe-2, in: 46th AIAA Aerospace Sciences Meeting and Exhibit, 2008, p. 399.
- [13] J. Riou, E. Garnier, C. Basdevant, Compressibility effects on the vortical flow over a 65° sweep delta wing, Phys. Fluids 22 (2010) 2–13, https://doi.org/10.1063/1. 3327286
- [14] M. Moioli, C. Breitsamter, K. Sørensen, Turbulence Modeling for Leading-Edge Vortices: an Enhancement Based on Experimental Data, AIAA SciTech Forum, Orlando, FL, 2020.
- [15] E. Tangermann, A. Furman, C. Breitsamter, Detached eddy simulation compared with wind tunnel results of a delta wing with sharp leading edge and vortex breakdown, in: 30th AIAA Applied Aerodynamics Conference, New Orleans, Louisiana, 2012.
- [16] S.-H. Peng, Verification of rans and hybrid rans-les modelling in computations of a delta-wing flow, in: 46th AIAA Fluid Dynamics Conference, 2016, p. 3480.
- [17] F.G. Schmitt, About Boussinesq's turbulent viscosity hypothesis: historical remarks and a direct evaluation of its validity, C. R., Méc. 335 (9–10) (2007) 617–627, https://doi.org/10.1016/j.crme.2007.08.004, https://hal.science/hal-00264386.
- [18] P.R. Spalart, Strategies for turbulence modelling and simulations, Int. J. Heat Fluid Flow 21 (3) (2000) 252–263.
- [19] B. Parmar, E. Peters, K.E. Jansen, A. Doostan, J.A. Evans, Generalized non-linear eddy viscosity models for data-assisted Reynolds stress closure, in: AIAA Scitech 2020 Forum, 2020, p. 0351.
- [20] S.B. Pope, A more general effective-viscosity hypothesis, J. Fluid Mech. 72 (2) (1975) 331–340, https://doi.org/10.1017/S0022112075003382.
- [21] C.L. Rumsey, J.-R. Carlson, T.H. Pulliam, P.R. Spalart, Improvements to the quadratic constitutive relation based on nasa juncture flow data, AIAAJ 58 (2020).
- [22] A. Hövelmann, A. Winkler, S.M. Hitzel, K. Richter, M. Werner, Analysis of vortex flow phenomena on generic delta wing planforms at transonic speeds, in: New Results in Numerical and Experimental Fluid Mechanics XII, Springer International Publishing, 2020, pp. 307–316.
- [23] S.R. Allmaras, F.T. Johnson, Modifications and clarifications for the implementation of the spalart-allmaras turbulence model, Seventh international conference on computational fluid dynamics (ICCFD7), vol. 1902, 2012, Big Island, HI.
- [24] M.L. Shur al, Turbulence modeling in rotating and curved channels: assessing the Spalart-Shur correction, AIAA J. 38 (5) (2000), https://doi.org/10.2514/2.1058.
- [25] F.R. Menter, Two-equation eddy-viscosity turbulence models for engineering applications, AIAA J. 32 (8) (1994) 1598–1605, https://doi.org/10.2514/3.12149.
- [26] P.R. Spalart, W.H. Jou, M. Strelets, S.R. Allmaras, Comments on the feasibility of les for wings, and on a hybrid rans/les approach, in: First AFOSR International Conference on DNS/LES, Ruston, LA, 1997.
- [27] F.R. Menter, Y. Egorov, The scale-adaptive simulation method for unsteady turbulent flow predictions. Part 1: theory and model description, Flow Turbul. Combust. 85 (1) (2010) 113–138, https://doi.org/10.1007/s10494-010-9264-5.

- [28] T. Gerhold, Overview of the hybrid rans code tau, in: N. Kroll, J.K. Fassbender (Eds.), MEGAFLOW - Numerical Flow Simulation for Aircraft Design, Springer, Berlin Heidelberg, 2005, pp. 81–92.
- [29] S. Langer, A. Schwöppe, N. Kroll, The dlr flow solver tau status and recent algorithmic developments, in: 52nd Aerospace Sciences Meeting, National Harbor, Maryland, USA, 2014.
- [30] O. Reynolds, IV. On the dynamical theory of incompressible viscous fluids and the determination of the criterion, Philos. Trans. R. Soc. Lond. A 186 (1895) 123–164.
- [31] A. Favre, The equations of compressible turbulent gases, Annual Summary Report AD0622097 (1965).
- [32] J.V. Boussinesq, Essai sur la théorie des eaux courantes, Impr. Nationale (1877).
- [33] P. Spalart, S. Allmaras, A one-equation turbulence model for aerodynamic flows, in: 30th Aerospace Sciences Meeting and Exhibit, 1992, p. 439.
- [34] M.L. Shur, P.R. Spalart, M.K. Strelets, A.K. Travin, A hybrid RANS-LES approach with delayed-DES and wall-modelled LES capabilities, Int. J. Heat Fluid Flow 29 (6) (2008) 1638–1649, https://doi.org/10.1016/j.ijheatfluidflow.2008.07.001.
- [35] P. Sagaut, S. Deck, M. Terracol, Multiscale and multiresolution approaches in turbulence, in: LES, DES and Hybrid RANS/LES Methods: Applications and Guideline, 2nd edition, Imperial Collegre Press, 2013, pp. 286–291, Ch. 7.
- [36] C.L. Rumsey, H.C. Lee, T.H. Pulliam, Reynolds-averaged Navier-Stokes computations of the nasa juncture flow model using fun3d and overflow, in: AIAA Scitech 2020 Forum, 2020, p. 1304.
- [37] T. Di Fabbio, E. Tangermann, M. Klein, Investigation of transonic aerodynamics on a triple-delta wing in side slip conditions, CEAS Aeronaut. J. (Feb 2022), https://doi.org/10.1007/s13272-022-00571-9.
- [38] I. Celik, Z. Cehreli, I. Yavuz, Index of resolution quality for large eddy simulations, 2005.
- [39] M. Klein, J. Meyers, B.J. Geurts, Assessment of les quality measures using the error landscape approach, in: Quality and Reliability of Large-Eddy Simulations, 2008, pp. 131–142.
- [40] S. Probst, T. Knopp, D. Francois, C. Grabe, T. Landa, R. Radespiel, Scale-resolving simulations of the streamwise vortex downstream of a delta wing, in: AIAA Scitech 2019 Forum, 2019, p. 0331.
- [41] A. Probst, S. Reuß, Progress in scale-resolving simulations with the dlr-tau code, in: Deutscher Luft- und Raumfahrtkongress, Braunschweig, Deutschland, 2016.
- [42] T. Di Fabbio, E. Tangermann, M. Klein, Investigation of leading-edge vortices on a triple-delta-wing configuration using scale-adaptive simulation, in: 33rd Congress of the International Council of the Aernoautilca Sciences, Stockholm, Sweden, 2022.
- [43] T. Di Fabbio, E. Tangermann, M. Klein, Investigation of Reynolds Stresses Prior to Vortex Breakdown on a Triple-Delta Wing at Transonic Condition, 12th International Symposium on Turbulence and Shear Flow Phenomena (TSFP12), Osaka, Japan, 2022.
- [44] G. Erlebacher, M.Y. Hussaini, C.W. Shu, Interaction of a shock with a longitudinal vortex, J. Fluid Mech. 337 (1997) 129–153, https://doi.org/10.1017/S0022112096004880
- [45] T. Di Fabbio, E. Tangermann, M. Klein, Analysis of the vortex-dominated flow field over a delta wing at transonic speed, Aeronaut. J. (2023) 1–18, https://doi.org/10. 1017/aer.2023.30.
- [46] M. Menke, I. Gursul, Unsteady nature of leading edge vortices, Phys. Fluids 9 (10) (1997) 2960–2966, https://doi.org/10.1063/1.869407.
- [47] P. Bradshaw, D. Ferriss, N. Atwell, Calculation of boundary-layer development using the turbulent energy equation, J. Fluid Mech. 28 (3) (1967) 593–616.